Available online at www.sciencedirect.com

ScienceDirect

Geochimica et Cosmochimica Acta 222 (2018) 704–728

Geochimica et Cosmochimica Acta

www.elsevier.com/locate/gca

Iron transformations during low temperature alteration of variably serpentinized rocks from the Samail ophiolite, Oman

Lisa E. Mayhew [a,*], Eric T. Ellison [a], Hannah M. Miller [a], Peter B. Kelemen [b], Alexis S. Templeton [a]

[a] Department of Geological Sciences, UCB 399, University of Colorado Boulder, Boulder, CO 80309, USA
[b] Lamont-Doherty Earth Observatory of Columbia University, 61 Route 9W, Palisades, NY 10964, USA

Received 13 February 2017; accepted in revised form 16 November 2017; available online 24 November 2017

Abstract

Partially serpentinized peridotites in the Samail ophiolite in the Sultanate of Oman currently undergo low temperature alteration and hydration both at shallow levels, with water recently in contact with the atmosphere, and at depth, with anoxic, reducing fluids. However, it is unclear how changes in the distribution and oxidation state of Fe are driving the production of energy-rich gases such as hydrogen and methane detected in peridotite catchments. We track the Fe transformations in a suite of outcrop samples representing a subset of the spectrum of least to most altered end-members of the Oman peridotites. We use microscale mineralogical and geochemical analyses including QEMSCAN, Raman spectroscopy, synchrotron radiation X-ray fluorescence (XRF) mapping, and electron microprobe wavelength dispersive spectroscopy. The less-altered peridotites possess a diversity of Fe-bearing phases including relict primary minerals (e.g. olivine, pyroxene, chromite) and secondary phases (e.g. serpentine and brucite). Raman spectroscopy and electron microprobe data (Si/(Mg + Fe)) indicate that much of the serpentine is significantly intergrown with brucite on the sub-micron scale. These data also indicate that the Fe content of the brucite ranges from 10 to 20 wt% FeO. The mineral assemblage of the highly reacted rocks is less diverse, dominated by serpentine and carbonate while olivine and brucite are absent. Magnetite is relatively rare and mainly associated with chromite. Goethite and hematite, both Fe(III)-hydroxides, were also identified in the highly altered rocks. Whole rock chemical analyses reflect these mineralogical differences and show that Fe in the partially serpentinized samples is on average more reduced (~0.40–0.55 Fe^{3+}/Fe_{Total}) than Fe in the highly reacted rocks (~0.85–0.90 Fe^{3+}/Fe_{Total}). We propose that olivine, brucite, chromite and, perhaps, serpentine in the less-altered peridotites act as reactive phases during low temperature alteration of the Oman peridotite. The pervasive oxidation of Fe(II) in the less-altered peridotites to Fe(III) in the most-altered peridotites during water-rock reaction in the subsurface of the Samail ophiolite may produce H_2 which will influence the development of microbial energy sources and habitats, and carbon cycling and sequestration within the (ultra)mafic ocean crust.

Keywords: Serpentinization; Oman ophiolite; Low temperature; Iron; Oxidation state; Synchrotron radiation; Raman spectroscopy

1. INTRODUCTION

The Samail ophiolite in the Sultanate of Oman is an excellent system to study low temperature alteration of ultramafic rocks because it is one of the best and largest exposures of oceanic crustal and shallow mantle rocks on Earth (e.g. Boudier and Coleman, 1981). The partially serpentinized peridotites experience modern day water/rock reactions at low temperatures (23–60 °C – Neal and Stanger, 1983, 1985; Kelemen et al., 2011; Streit et al., 2012; Miller et al., 2016). The rocks interact with fluids with

* Corresponding author.
E-mail address: mayhewl@colorado.edu (L.E. Mayhew).

https://doi.org/10.1016/j.gca.2017.11.023
0016-7037/

diverse chemistries that include rainwater, Mg^{2+}/HCO_3^- -rich fluids, and Ca^{2+}/OH^- -rich fluids (Barnes et al., 1978; Neal and Stanger, 1985). Moderately alkaline (pH ~ 8–9) Type I fluids (terminology from Barnes and O'Neill, 1969; Neal and Stanger, 1985), and hyperalkaline (pH ~ 10–12) Type II fluids rich in H_2 and CH_4 (Barnes et al., 1978; Neal and Stanger, 1983, 1985; Clark and Fontes, 1990; Kelemen and Matter, 2008; Kelemen et al., 2011) are produced by modern day alteration of the ultramafic peridotite.

Iron redox transformations that occur during low temperature (<150 °C) water/rock reactions are a key component of the dynamic chemistry and potential habitability of serpentinizing systems (e.g. Sleep et al., 2004; McCollom and Bach, 2009; Klein et al., 2014). The oxidation of Fe(II) in (ultra)mafic minerals to Fe(III) in secondary phases will reduce water to H_2 gas under anoxic, reducing conditions (e.g. Neal and Stanger, 1983). Hydrogen gas is essential to biologic processes (e.g. Nealson et al., 2005), is one of the most important electron donors for extant chemolithotrophs (Nisbet and Sleep, 2001), and may have been one of the earliest sources of energy on Earth (e.g. Sleep et al., 2004; Russell et al., 2010). Initial experimental and modeling studies of the speciation and partitioning of Fe into the diversity of secondary mineral phases that can form during low temperature serpentinization (<150 °C) have been conducted (Klein et al., 2009; McCollom and Bach, 2009; Mayhew et al., 2013; Bach, 2016). Yet, relatively little is known about the conditions and processes under which different secondary minerals form and accommodate Fe at low temperature. It is often assumed that during serpentinization all Fe(III) is accommodated by magnetite formation (McCollom and Bach, 2009; Cannat et al., 2010; Malvoisin et al., 2012a). Significant Fe(III) substitution into serpentine (up to 70%) has been documented in mid-ocean ridge and continental margin systems (O'Hanley and Dyar, 1993; Andreani et al., 2008; Klein et al., 2009; Evans et al., 2009; Streit et al., 2012; Klein et al., 2014), as well as experimental systems (Seyfried et al., 2007; Marcaillou et al., 2011). Yet, the significance of Fe(III) partitioning into serpentine for H_2 production has been debated (Beard and Frost, 2016). The production of Fe-rich serpentine is often accompanied by the partitioning of Fe(II) into brucite and occurs at low temperatures (150–250 °C) and water-rock ratios (Moody, 1976a,b; Sleep et al., 2004; Bach et al., 2006; Seyfried et al., 2007; Klein et al., 2009; McCollom and Bach, 2009; Klein et al., 2014; Bonnemains et al., 2016). A small degree (up to 10% Fe) of Fe(III)-partitioning into brucite has recently been reported (Beard and Frost, 2016). This differential partitioning of Fe has a significant impact on the possible extent of Fe(II) oxidation and subsequent H_2 generation during water/rock reactions.

The diversity of geochemical conditions and fluid compositions within the Samail ophiolite result in a variety of Fe oxidation pathways, making the ophiolite a natural laboratory in which to investigate the geochemical reactions that give rise to the mineral assemblages and energy-rich by-products associated with low temperature aqueous alteration of ultramafic rocks. Previous characterization of rocks of the Oman ophiolite has revealed that ~90% of Oman peridotites are harzburgites (~85% olivine, 10–15% orthopyroxene, 5% spinel, ≪1% clinopyroxene) while ~10% are dunites (>90% olivine, 5–10% spinel, ≪1% clinopyroxene) that occur in isolated lenses (Boudier and Coleman, 1981; Godard et al., 2000; Monnier et al., 2006; Hanghoj et al., 2010). All Oman peridotites collected from outcrops exhibit some degree of alteration (Kelemen et al., 2011) ranging from minimally serpentinized (~30–60%; Hanghoj et al., 2010; Boudier et al., 2010) to entirely serpentinized and carbonated (e.g. Boudier et al., 2010; Streit et al., 2012; Falk and Kelemen, 2015). Notably, abundant Fe-bearing serpentine, with an Fe(III) component, has been observed in the serpentinized peridotite (Streit et al., 2012; Miller et al., 2016) variably intermixed with Fe-bearing brucite (Miller et al., 2016). A variety of possible formation mechanisms exist to explain the observed alteration phases, which have very different implications for H_2 production. For instance, the hydration of primary olivine to serpentine and other Fe(III)-bearing phases may generate H_2, while the transformation of Fe(III)-oxides to magnetite would consume H_2.

The objective of this current work is to characterize low temperature Fe transformations and mineral alteration pathways recorded in serpentinites from the Samail ophiolite in Oman. A detailed, microscale mineralogical analysis of the less-altered Oman peridotites provides insights into the mineral assemblages and Fe chemistry of partially altered serpentinites that still possess the potential for further oxidation. Characterization of highly altered end-members of the Oman peridotites provides possible end points of alteration for comparison. Combining bulk and microscale geochemical characterization techniques and comparison of least- to most-altered rocks allows us to assess the iron mineralogy associated with low temperature serpentinization, which gives insight into possible H_2-generating and consuming reactions within the Oman ophiolite.

2. METHODS

2.1. Serpentinite samples from the Oman ophiolite

Twelve serpentinite rock samples collected from surface outcrops of the Oman ophiolite were characterized in this study. At the hand sample scale, the samples vary significantly in lithology and extent of alteration. Those that appear to be less-altered include samples OM94-61, a harzburgite collected from the Wadi Tayin massif (Hanghoj et al., 2010), (OM94-61 was not analyzed by bulk techniques because we did not have access to a bulk rock sample.); OM95-35, a dunite from the Samail massif; OM14-06 and OM14-07 dunites from Wadi Lufti; OM14-05 a harzburgite/dunite from Wadi Lufti; OM14-08 a characteristic harzburgite from Wadi Quafifa; OM14-10 a harzburgite fromWadi Dhuli. The highly altered rocks investigated here include OM08-01, OM08-206A and 206D, and OM09-129 which were previously studied by Streit et al. (2012) and OM14-11, a completely serpentinized harzburgite.

2.2. X-ray diffraction

Rocks were powdered with a mortar and pestle for bulk analyses. X-ray diffraction (XRD) analyses were conducted on a Bruker D2 Phaser with a Cu Kα radiation ($\lambda = 1.5418$ Å) source operated at 30 kV and 10 mA. Data was obtained across a 2θ range of 5 or 15–65° using a Lynxeye 1D detector with a step size of 0.02° and collection time of 1 s per step. Despite the variation in 2θ range, all data is diagnostic for the key mineral phases. The XRD spectra were semi-quantitatively fit using the Bruker DiffracEva program and results were compared to the RRUFF database (Lafuente et al., 2015).

2.3. Total Fe by XRF

X-ray fluorescence (XRF) analyses of whole rock samples were conducted to obtain total Fe content (USGS, Boulder, CO). Homogenized samples were milled to <1 mm and baked in acid-washed (trace metal-clean) porcelain crucibles in a Thermolyne 6000 muffle furnace at 550 °C for 2 h and at 925 °C for 45 min. Sample mass was measured before and after baking to calculate loss on ignition (LOI). Aliquots of 0.8000 grams (±0.0005 g) of each sample was mixed with 8.0000 grams of Fluxite (GF-65-5I, Premier Lab Supply) and transferred to platinum crucibles. Fused beads were made using a VFD 400 Phoenix fuser (XRF Scientific) and stored in a desiccator until analysis. Beads were analyzed with a Siemens SRS 3000 sequential X-ray fluorescence spectrometer equipped with a rhodium X-ray tube and flow counter and scintillation counter detectors. Each bead was masked to a 34 mm diameter, analyzed in a vacuum in triplicate and the concentrations averaged. Drift correction was performed <5 days before the samples were analyzed. Total Fe content was calculated by measuring the intensity of the Fe Kα-1 line (57.51 degrees 2Θ) at 60 kV and 25 mA with a 0.15 degree collimator and a LiF200 crystal. At least one standard reference material was analyzed with the samples as QA/QC at a frequency of approximately 10% of the total number of samples, and several sample beads were analyzed multiple times to verify instrument analytical reproducibility.

2.4. Fe(II)O by titration

Analyses of whole rock FeO contents were conducted at Actlabs (Ontario, Canada). Digestion by ammonium metavanadate and hydrofluoric acid were conducted in an open system and ferrous ammonium sulfate was added prior to titration with potassium dichromate. FeO contents were used to calculate Fe^{3+}/Fe_{Total}.

2.5. QEMSCAN

Mineral identification and semi-quantitative mineral abundances of samples in thin sections were determined using QEMSCAN scanning electron microscopy which integrates energy dispersive X-ray spectroscopy with back scatter electron intensities to identify mineral phases (Hoal et al., 2009). Analyses were conducted at the Advanced Mineralogy Research Center at the Colorado School of Mines. The instrument operated at an accelerating voltage of 25 kV, a 5 nA current, and a 1 μm beam size with a step size of 5 μm.

2.6. Raman spectroscopy

Micro-Raman spectra and hyperspectral maps were collected using a Horiba LabRAM HR Evolution Raman spectrometer equipped with a 100 mW 532 nm frequency-doubled Nd:YAG laser. The laser beam was attenuated to 10–50% of the power at the source and focused through a 50x (0.75 NA) or 100x (0.90 NA) objective lens, yielding a spatial resolution of ~1–2 μm for point spectra. The confocal pinhole was set to 100 μm. Additionally, the laser passes through a depolarizer prior to interacting with the sample to reduce orientation effects. A Si-based CCD detector (1024 × 256 pixels) was employed for all data collection. The spectrometer was calibrated using the 520 cm^{-1} Raman peak of Si prior to analysis. For mineral identification, spectra were collected from 100 to 1750 cm^{-1} (fingerprint region) using a 600 lines/mm grating for a spectral resolution full width at half maximum (FWHM) of 4.5 cm^{-1}. For detection of brucite, spectra were collected from 3550 to 3750 cm^{-1} (OH stretch region) using a 1800 lines/mm grating giving a spectral resolution of 1.5 cm^{-1}. Hyperspectral maps were collected as for mineral identification, except that for most maps the laser spot was rapidly scanned over a larger mapping pixel area (4–5 μm) in order to increase the sample area that was feasible to image. Spectral data were corrected for instrumental artifacts and baseline-subtracted using a polynomial fitting algorithm in LabSpec 6 (Horiba Scientific). The main spectral components present in the hyperspectral maps were identified by either Multivariate Curve Resolution (Andrew and Hancewicz, 1998), or by hand picking area-averaged component spectra from within the map. Spectral components identified by MCR were verified by examining the actual spectral data from the high score pixels. Maps of end member spectral component distributions were generated from classical least squares fitting of the hyperspectral map data. End member spectral components were identified by comparison to the RRUFF spectral database (Lafuente et al., 2015).

2.7. X-ray spectroscopy

Bulk Fe K-edge XANES spectra (X-ray Absorption Near Edge Structure) of powdered rock samples were collected on Beamline 4-1 at the Stanford Synchrotron Radiation Lightsource (SSRL). The incident energy was selected with a Si (220) $\phi = 0$ monochromator. Data was collected from 6882 to 7082 eV with a step size of 10 eV, from 7082 to 7108 eV with a step size of 0.4 eV, from 7108 to 7118 eV with a step size of 0.1 eV, from 7118 to 7142 eV with a step size of 0.35 eV, and from 7142 eV to 7505 eV with a step size increasing from 2 to 10 eV. Fluorescence intensities at each energy were collected with a PIPS detector. Two to five scans were collected for each sample and each scan was individually calibrated by shifting the first inflection point of a Fe^0 foil standard transmission spectrum that

was collected simultaneously with that scan to 7112 eV. Spectra collected from the same sample were averaged, background subtracted using a linear fit to the pre-edge region (6882–7050 eV) and a quadratic fit to the post-edge region (7222–7505 eV) and normalized to the edge step height. Data treatment was conducted in the statistical computing software, R (R Development Core Team, 2013).

Spatially-resolved Fe K-edge XANES spectroscopy (X-ray Absorption Near Edge Structure) and X-ray fluorescence (XRF) mapping was conducted using a synchrotron radiation-based hard-X-ray microprobe at Beamline 2-3 at the SSRL. Data collection occurred with the SPEAR3 accelerator ring containing ~500 mA at 3.0 GeV. A Si (111) double crystal monochromator (energy resolution of 0.7 eV at the Fe K-edge for a beam height of 200 μm) was used for selection of the incident energy. Trace element (Mn, Zn, Cr, Ni, Cu) and major ion (Ca, Fe, Si) μXRF maps were collected at 11 keV with a focused spot size and pixel step-size of 2 × 2 μm. Maps were generated in a continuous raster scanning mode using a single-element vortex detector capable of reading several million counts per second. All windowed counts for each element extracted from the full X-ray fluorescence spectra were normalized to the intensity of the incident X-ray beam (I_0). Dwell times were 25–50 ms. Maps and spectra were calibrated using the first inflection of an Fe^0 foil at 7112 eV. Fe K-edge XANES spectra were collected from 6882 to 7520 eV. A high resolution step size (0.1 eV) was used through the pre-edge (7108–7118 eV) region with a dwell time of 3 s. Data was collected from 7118 to 7142 eV with a step size of 0.35 eV and from 7142 to ~7520 eV with a step size increasing from 0.35 to 11 eV. The full spectrum was used for background subtraction and normalization to unit step edge as stated in the methods above. Micro-XANES spectra were fit from 7110 to 7150 eV with linear combinations of Fe model compounds (Mayhew et al., 2011 Supporting Information). All fits were done using the 'Cycle Fit' function in SIXPACK (Webb, 2005). All models were fit individually as one-component fits and then the fit cycle was repeated for two-component fits using the best one-component model compound paired with the remaining model compounds. This process is repeated until adding an additional component no longer decreases the R^2 value by 10% or greater.

2.8. Electron microprobe

A JEOL JXA-8600 electron microprobe (EMP) (University of Colorado at Boulder) equipped with 4 wavelength-dispersive spectrometers (WDS) was used for quantitative chemical analysis of component mineral phases. Spot analyses of polished, carbon coated thin sections were performed at a current of 10 nA, accelerating voltage of 15 keV, and beam diameter of 10 μm to minimize damage to the hydrated phases. Major elements (Si, Al, Mg, Fe) were analyzed and quantified against natural standards. Prior to WDS analyses, an electron dispersive spectroscopic (EDS) measurement was collected to identify the diversity of elements present in the pixel to be analyzed to ensure that no major component of the pixel was omitted from the WDS analysis.

3. RESULTS

3.1. Bulk mineralogy and geochemistry

3.1.1. Powder X-ray diffraction

There are two distinct groups of bulk XRD spectra: complex spectra with both primary and secondary phases and spectra that mainly consist of serpentine +/- carbonate. Peaks matching olivine (forsterite) were detected in the spectra of samples OM95-35, OM14-05, -06, and -08 (Fig. 1). Peaks of pyroxene (enstatite) were identified in OM14-08 and to a lesser degree in samples OM14-11, OM09-129, OM08-206A/D. All spectra possess prominent lizardite (serpentine group mineral) peaks, whereas a detectable brucite (secondary Mg-hydroxide) peak was limited to samples OM95-35, OM14-05 and -06. The spectrum of sample OM14-07 is unique with a peak at $2\theta = 12°$ that is indicative of a hydrotalcite group mineral. Samples OM08-01, OM08-206A/D, and OM09-129 also have prominent carbonate (calcite; magnesite) peaks.

3.1.2. Whole rock total Fe and FeO

Whole rock XRF analyses show total Fe contents that range from ~3 to 7%Fe (Table S1). Samples OM95-35, OM14-05, -06, -07, and -08 have an average of 6.4%Fe while samples OM08-01, OM08-206A/D, OM09-129, and OM14-11 have an average of 4.6%Fe. These two populations of samples also differ markedly in their bulk FeO content. The less altered peridotites have an average of 3.8% FeO while the more highly altered rocks have an average of 0.6%FeO. Ratios of Fe^{3+}/Fe_{Total} were calculated and range from ~0.4 to 0.9 (Table S2). This data also falls into two distinct groups, samples with values ranging from ~0.4 to 0.5 and samples with values close to 0.9. These two groups generally correlate with those previously defined as less vs. more altered except for OM14-07 which appears to be less-altered but has $Fe^{3+}/Fe_{Total} \sim 0.9$.

3.1.3. Bulk Fe speciation by Fe K-edge XANES

The same powders analyzed by XRD were also analyzed using synchrotron radiation based XANES spectroscopic techniques. Overplotting the bulk Fe K-edge XANES spectra from all samples reveals a separation in edge position between the different samples (Fig. 2a). The least altered dunite (OM95-35) has the lowest energy edge and peak position. Samples OM14-06 and -07 are similar to OM95-35 while sample OM14-10 has intermediate edge and peak positions. Spectra of samples OM08-01, OM08-206A/D, OM09-15, OM09-129, OM14-05,-08, and -11 have higher energy edge and peak positions suggesting that the Fe in these samples is more oxidized (Fig. 2a). Least-square fits to the XANES spectra reveal the dominant Fe mineral speciation at the bulk scale. Olivine is a component invoked in only three samples (OM95-35, OM14-06, -07), these samples also have major contributions from serpentine ± minor contributions from other phases including brucite and pyroxene (Table S2). Fits to spectra from all other samples are dominated by Fe(III)-oxides and serpentine ± contributions from chromite and other Fe-phyllosilicates (Table S2).

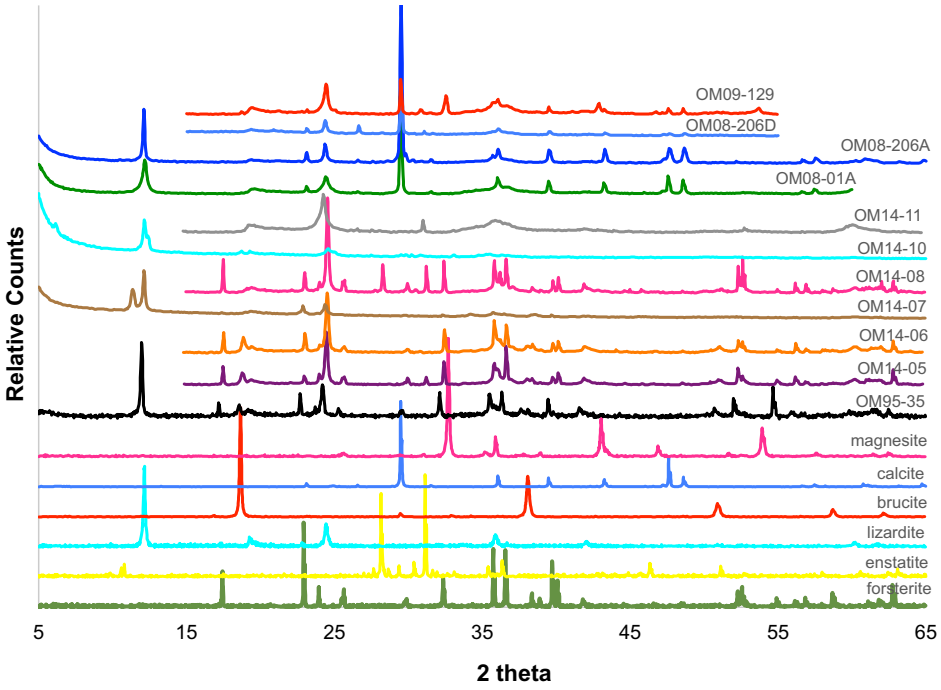

Fig. 1. X-ray diffraction spectra of bulk powders of Oman serpentinites plotted with reference spectra from the RRUFF database.

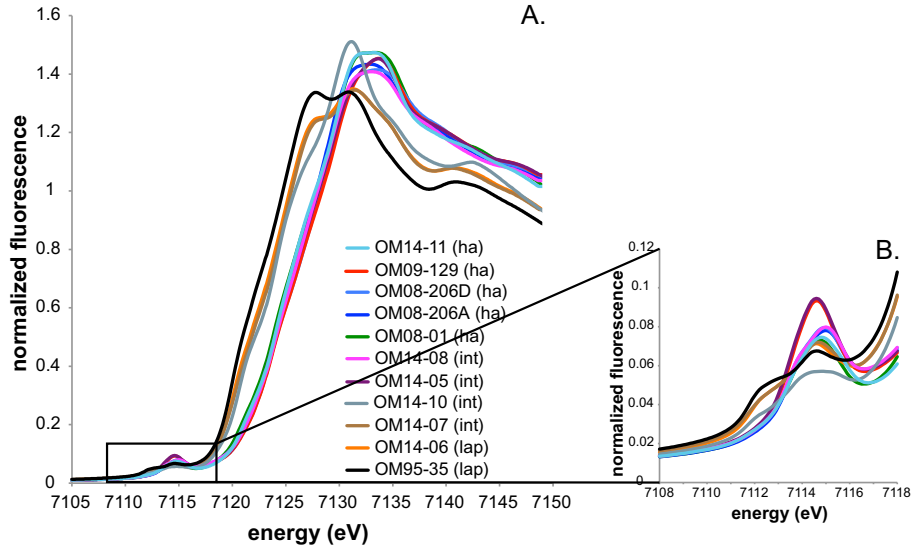

Fig. 2. Powdered bulk rock samples of Oman peridotites were measured using synchrotron radiation XAS. (A) Fe K-edge XANES spectra show a shift in edge and peak position to higher energies with increasing degree of alteration, suggestive of a greater degree of oxidation of Fe in more highly altered rocks. (B) Similarly, in the pre-edge region of the spectra, a higher intensity peak at lower energies is present at lower extents of alteration whereas rocks that experienced greater alteration have a much higher intesity peak at higher energies; indicative of more oxidized Fe with a greater component of tetrahedrally coordinated Fe(III). Letters after the sample names indicate whether samples are less-alerted (lap) or highly altered (ha) peridotites or if they have attributes of both (int = intermediate).

We attempted quantitative analysis of the pre-edge peak of Fe K-edge XANES spectra to determine the Fe^{3+}/Fe_{Total} in the bulk samples (e.g. Andreani et al., 2013; Munoz, 2013). Sample OM95-35 appears to have ~0.25 Fe^{3+}/Fe_{Total} whereas OM14-06 and OM14-07 have ~0.40 Fe^{3+}/Fe_{Total} and OM14-10 has ~0.50 Fe^{3+}/Fe_{Total} while the highly altered, carbonate-bearing rocks have ~0.85–1.00 Fe^{3+}/Fe_{Total} (Fig. S1). However, because the analyses take into account all of the Fe-bearing phases within the rock samples, including chromite which possesses tetrahedrally coordinated Fe(II), the presence of these phases pull the data towards an area of the variogram that is not

calibrated (Fig. S1). Thus, quantification of bulk Fe^{3+}/Fe_{Total} using this technique is not robust. However, the values (± the 10% error associated with the technique (Wilke et al., 2001)) are generally consistent with calculations of Fe^{3+}/Fe_{Total} from whole rock chemical analyses. Visual inspection of the pre-edge feature reveals higher intensity peaks at lower energies for samples OM95-35, OM14-06, -07, and -10 versus higher intensity peaks at higher energies for the other samples (Fig. 2b). Notably, the highly altered rocks also appear to have a greater contribution of tetrahedrally coordinated Fe(III) based on the higher integrated intensity of the pre-edge.

3.2. Microscale mineralogy

3.2.1. QEMSCAN

Microscale characterization techniques were applied to a subset of the sample suite due to cost and time constraints. QEMSCAN was used to obtain coarse scale (5×5 μm^2), qualitative mineralogical insights into relatively large map areas (~90–230 mm^2). Due to its relatively coarse scale and qualitative approach to mineral identification, QEMSCAN data was not used for detailed interpretation of the sequence or process of serpentinization instead, it is used mainly for bulk mineral identification and as a tool to identify areas of interest for more detailed Raman spectroscopic analyses. Semi-quantitative mineral abundances obtained from QEMSCAN analyses of thin sections show that olivine is the most abundant Fe(II)-bearing relict primary phase in the samples studied here (~40% by area in the dunite OM95-35; ~25–35% in the harzburgites OM94-61 and OM14-05) (Table 1). Samples OM95-35, OM14-05, and OM94-61 have ~55–65% serpentine and retain a significant proportion of relict olivine A typical serpentine mesh texture surrounding relict olivines is observed in these rocks (Fig. 3). Relict pyroxene grains, which appear to be more pristine than the olivine crystals, are larger and more abundant in the harzburgites (OM94-61 and OM14-05) than in the dunite (OM95-35) (~1–2% vs. 0.22%).

Chromite abundances should be considered rough approximations because of the large size of the grains (~1–3 mm) and the microscale nature of the QEMSCAN technique. The inclusion or exclusion of a small number of chromite grains would significantly change the calculation of chromite abundance thus the microscale analyses may not be representative of the bulk rock. Considering this limitation, chromite appears more abundant in the harzburgites than in the dunite (~1% vs. 0.21%) and abundances are comparable to the average of 0.6% spinel reported by Monnier et al. (2006). Many of these chromites, especially in the harzburgites, are large (~1–3 mm) and similar in appearance to the holly leaf-shaped spinels interpreted to be a primary igneous phase by Monnier et al. (2006). In all samples, the chromites are extensively fractured (Fig. 3). Other minor phases that were detected include talc, chlorite, and carbonates. Brucite, which was detected by both bulk XRD and XANES, was not observed in QEMSCAN data. Similarly, magnetite, which was observed to be present in some samples, using other microscale techniques (see Section 3.2.2; and by reflected light microscopy) was not definitively detected by QEMSCAN. This is because of the relatively coarse scale of the QEMSCAN analyses.

Olivine is absent from all of the highly altered rocks. Relict pyroxenes are highly fractured and thoroughly cross-cut by serpentine (bastite) in samples OM08-206D and OM08-206A (Fig. 4a, compare to Fig. 3). When considering all of the mineral phases detected by QEMSCAN, the highly altered rocks that were analyzed consist of ~45–65% serpentine by area and ~20–40% carbonate minerals (Fig. 4; Table 1). Carbonate occurs mainly in extensive vein networks suggesting that carbonate results from the addition of CO_2-rich fluids and does not represent direct, in place alteration of the peridotite. If we consider this end-member scenario and renormalize the mineral percents with carbonate omitted, the percent of serpentine in the highly altered rocks increases to ~65–95%. Sample OM09-129 has a mesh texture in which serpentine surrounds carbonate,

Table 1
Normalized modal abundance (area percent) of each mineral as obtained by QEMSCAN analyses.

Mineral phase	OM95-35	OM94-61	OM14-05	OM08-01A	OM08-206A	OM08-206D	OM09-129	OM94-69
Olivine	42.64	25.56	33.59	0	0	0	0	4.22
Serpentine	56.21	63.89	61.37	61.22	43.02	42.53	65.94	91.87
Calcite	0	0.37	0	36.50	42.40	33.32	21.41	0
Pyroxene	0.22	2.05	1.27	0.85	7.39	12.33	5.63	1.63
Talc	0.02	5.79	1.74	0.03	2.29	2.08	0	0.02
Quartz	0.02	0.01	0.04	0.02	1.64	3.32	0.03	0
Chromite	0.31	0.79	0.87	0.13	0.24	0.28	0.46	0.69
Other carbonates	0.45	0.37	0.18	0.00	0	0	0	0.70
Chlorite	0.06	0.41	0.53	0.11	0.01	0.01	0.28	0.26
Amphibole	0	0.01	0	0	0.13	0.25	0	0
Fe-oxides[a]	0	0	0	0	0.05	0.02	0.20	0.01
Others	0	0.27	0.13	0.20	0.32	1.00	3.42	0.12
Background	0.07	0.49	0.29	0.94	2.51	4.88	2.50	0.49
Total	100.00	100.01	100.01	100.00	100.00	100.02	99.87	100.01
Serpentine[b]	56.46	64.36	61.47	96.41	74.69	63.76	84.04	92.51

[a] Different phases within the mineral group Fe-(hydr)oxides are not distinguishable by this technique.
[b] Serpentine normalized when carbonate is omitted from the total.

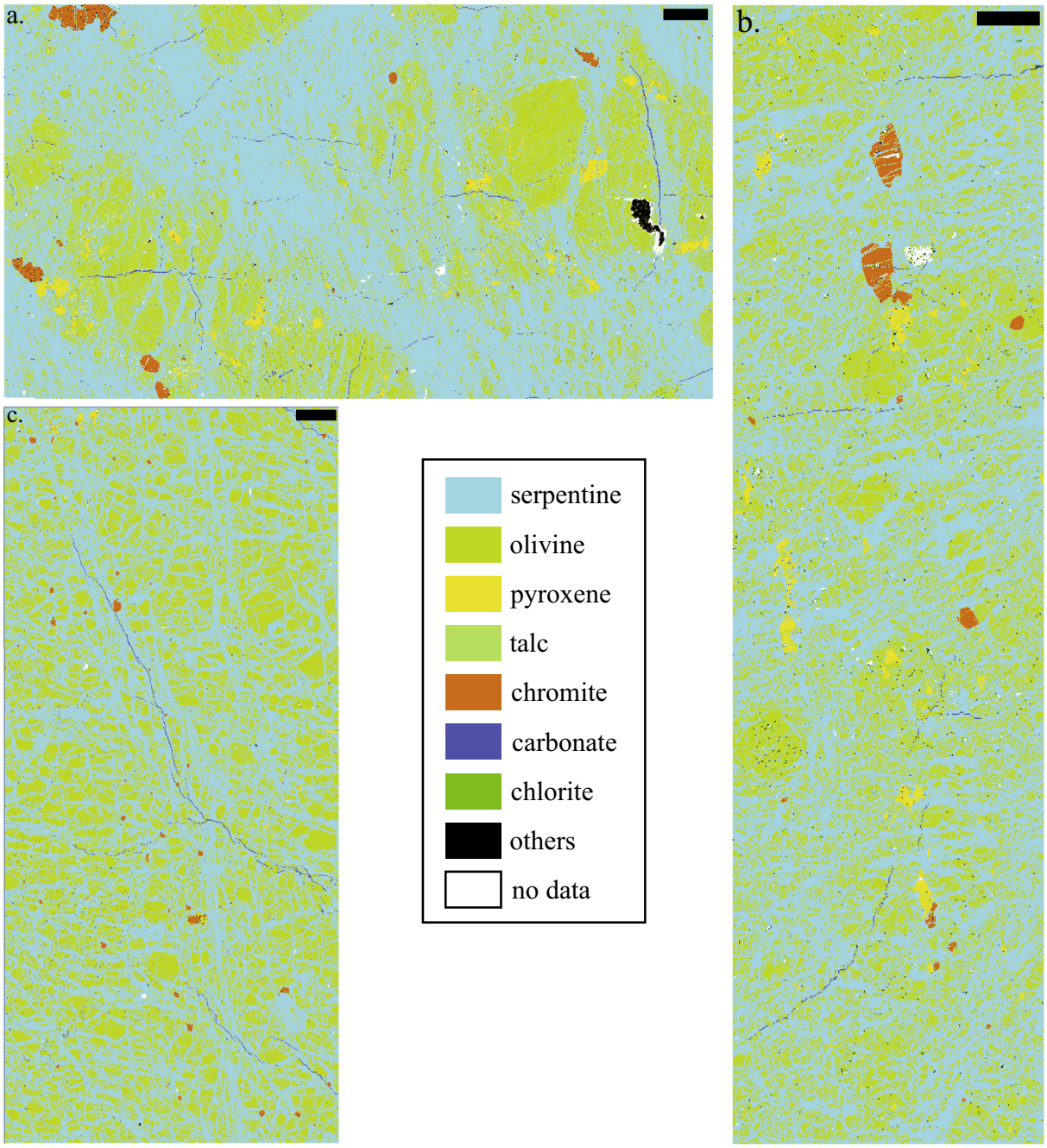

Fig. 3. QEMSCAN mineralogy maps of less-altered Oman serpentinites. (a) OM94-61, (b) OM14- 05, and (c) OM95-35. Scale bar for all maps represents 1000 um.

not olivine (Fig. 4b). Chromites are less abundant in the highly altered rocks. Other minor phases that were detected include talc, quartz, chlorite, and Fe(III)-oxides (Table 1).

3.2.2. Raman microspectroscopy

Raman spectroscopy reveals the presence and distribution of more rare, but potentially important, mineral phases. Mapping within the OH stretch region (3550–3750 cm^{-1}) revealed that the majority of serpentine in OM95-35 (dunite) is mixed with brucite ($Mg_xFe_{1-x}(OH)_2$) (Fig. 5). Brucite does not occur as a pure phase in OM95-35; it is always mixed with serpentine. Distinct areas of pure brucite were detected in OM14-06, also a dunite (Fig. 5f). Brucite is also observed in OM14-05, a harzburgite/dunite, though in contrast to the dunites, it is less abundant and is often preferentially localized along the rims of relict olivine grains (Fig. 5l). We detected brucite mixed with serpentine in a few discrete locations in OM94-61 (Fig. 5o); however, brucite was not found within the map area. We did not find brucite in association with magnetite.

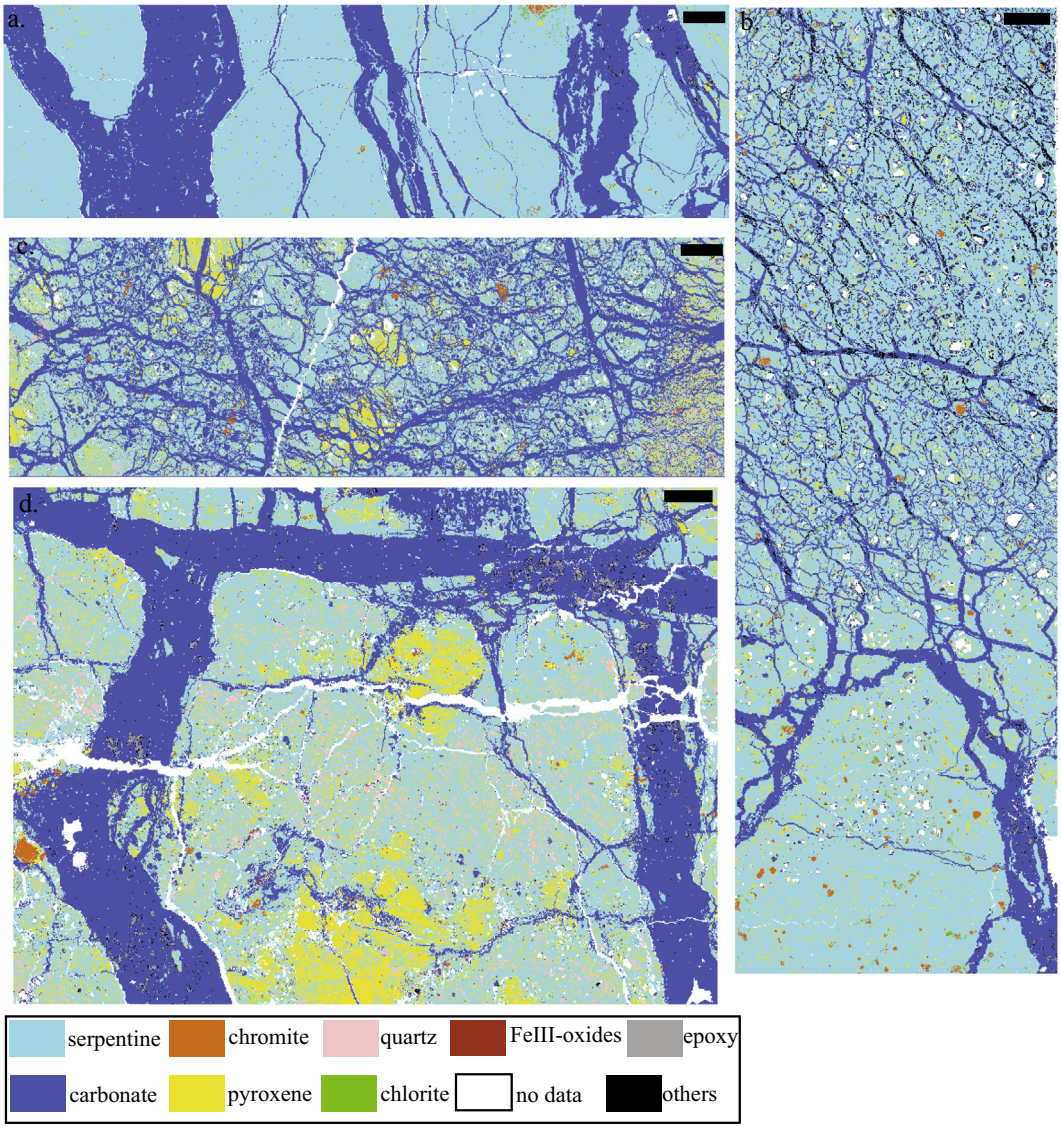

Fig. 4. QEMSCAN mineralogy maps of highly altered Oman serpentinites. (a) OM08-01, (b) OM09-129, (c) OM08-206A, and (d) OM08-206D. Scale bar for all maps represents 1000 um.

An enigmatic phase with a unique, but as yet unidentified, Raman spectrum (unknown, Fig. 5e) is distributed at the interface of olivine grains and associated brucite in OM14-06 (Fig. 5f). Elemental analysis of this phase, by electron dispersive spectroscopy, did not detect the presence of any elements other than Mg and Fe, although oxygen, water and carbon are not robustly detectable with this instrument. The mineralogical identity of this phase remains unknown.

Actinolite and talc were distinguished from serpentine, in OM94-61, a harzburgite (Fig. 5n). Magnetite, which was not robustly detected using QEMSCAN, was detected by Raman in dunites at the rims of chromite grains and in association with serpentine veins (Fig. 5f). Magnetite was also detected in harzburgite in association with actinolite (Fig. 5n). Rare instances of garnet (probably hydrogrossular), amphibole, and clinochlore were found in association with co-localized pyroxene and chromite in OM95-35 (Fig. 5a and b).

In highly altered rocks, brucite was not detected, even when carefully examining the OH stretch region of Raman spectra. In contrast, much of the serpentine in OM08-206D is extensively mixed with Fe(III)-(hydr)oxides, specifically goethite (Fig. 6a and b). This causes the serpentine to appear dark brown in plane polarized light images (see Fig. 8). Similarly, an Fe(III)-(hydr)oxide phase is found in veins and cores of the mesh texture in OM09-129 (Fig. 6c and d).

Chromite in sample OM08-206D appears relatively unaltered. In contrast, only the core of the chromite in OM09-129 is identified as chromite by Raman spectroscopy. The material surrounding the core (~20–70 μm thick) is a Cr-rich magnetite which itself is surrounded by

a much thinner (~10 μm) layer of clinochlore, an Fe-bearing chlorite, such as detected by QEMSCAN in this sample. In sample OM08-01A, what morphologically appears to be a chromite grain is identified as a Cr-rich magnetite with no true chromite remaining (Fig. 6e and f; see Fig. 8). Quartz was also detected in OM08-206D as observed by previous researchers using electron microprobe (Streit et al., 2012).

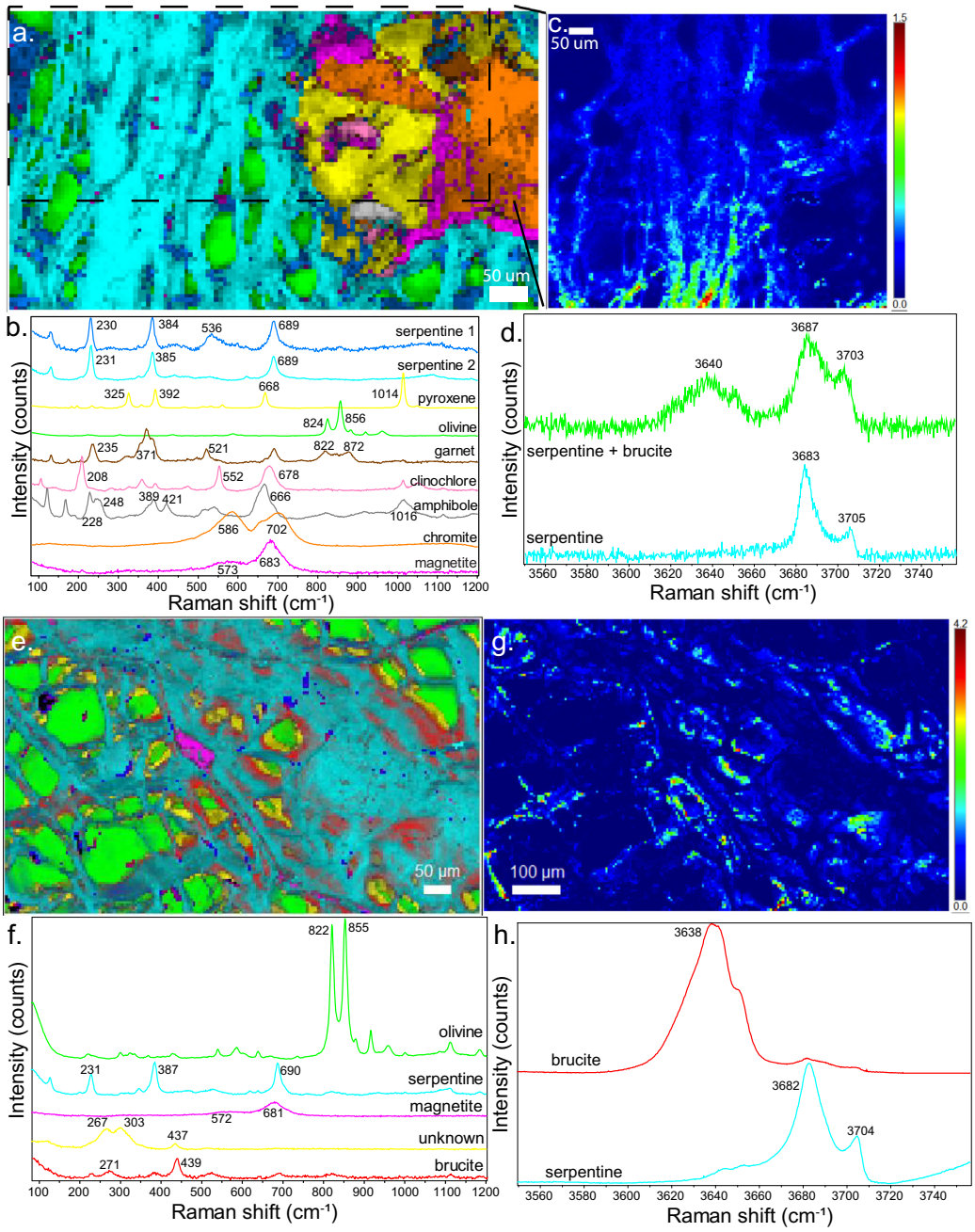

Fig. 5. Hyperspectral Raman maps of the distribution of minerals in less altered Oman peridotites (a) OM95-35, (e) OM14-06, (i) OM14-05 and (m) OM94-61. Raman spectra of mineral components used in the classical least squares fits are shown in (b) OM95-35, (f) OM14-06, (j) OM14-05 and (n) OM94-61. Colors of the maps correspond to colors in the spectra plot. The distribution of brucite is shown in (c) OM95-35, (g) OM14-06, and (k) OM14-05. The colorramp represents the coefficient by which the brucite spectrum is multiplied, higher values indicate a greater amount of brucite. The area of (c) is indicated by the dashed black box in (a) though (c) extends above the upper limit of (a). Spectra of the OH-stretch region distinguish between brucite, serpentine, and a mixture of the two (d) OM95-35, (h) OM14-06, (l) OM14-05 and (o) OM94-61. It was not possible to map the distribution of brucite in OM94-61 but point spectra from the OH-stretch region (o) verified the presence of brucite mixed with serpentine localized around olivine grains. (For interpretation of the references to colour in this figure legend, the reader is referred to the web version of this article.)

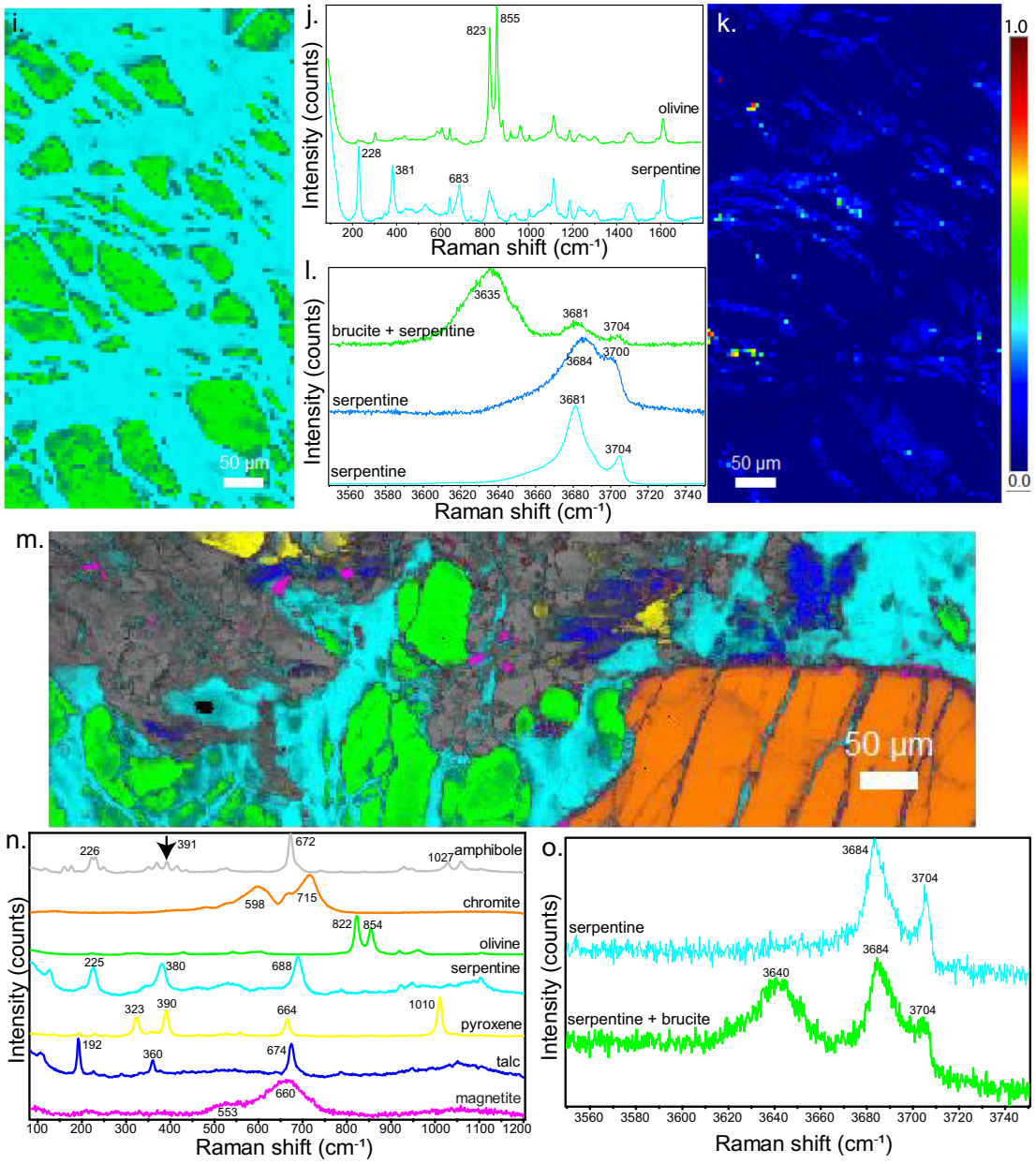

Fig 5. *(continued)*

3.3. Mineral chemistry

3.3.1. XRF element maps

Synchrotron radiation μXRF elemental maps were used to determine the presence, and relative concentration, of Fe in distinct mineral phases within Oman serpentinites. In samples OM95-35, OM94-61, OM14-05, and -06, Fe is held in the primary phases olivine and chromite ± minor pyroxene (Fig. 7). Iron is also present in serpentine, and in magnetite when it is present. Other minor secondary phases (e.g. talc, chlorite, and amphibole) appear to possess very little iron (Fig. 7).

In the highly altered rocks, iron is present mainly in serpentine, as serpentine constitutes the bulk of the rock. However, the iron content of the relict olivine and chromite is greater than that of the serpentine (Fig. 8). Streit et al. (2012) observed Fe zoning, with high Fe concentrations in serpentine along grain boundaries with quartz in samples OM08-206A and OM08-206D. Additionally, iron is concentrated in secondary Cr-rich magnetites and Fe-oxides while there is very little iron in the carbonate minerals.

3.3.2. Iron content of minerals determined from electron microprobe and Raman analysis

Wavelength dispersive spectroscopy was used to quantitatively determine the chemical formulas of key mineral phases (Table 2). Olivine varies from 0.08 to 0.10 average XFe (molar Fe/molar Fe + molar Mg) with minor substitu-

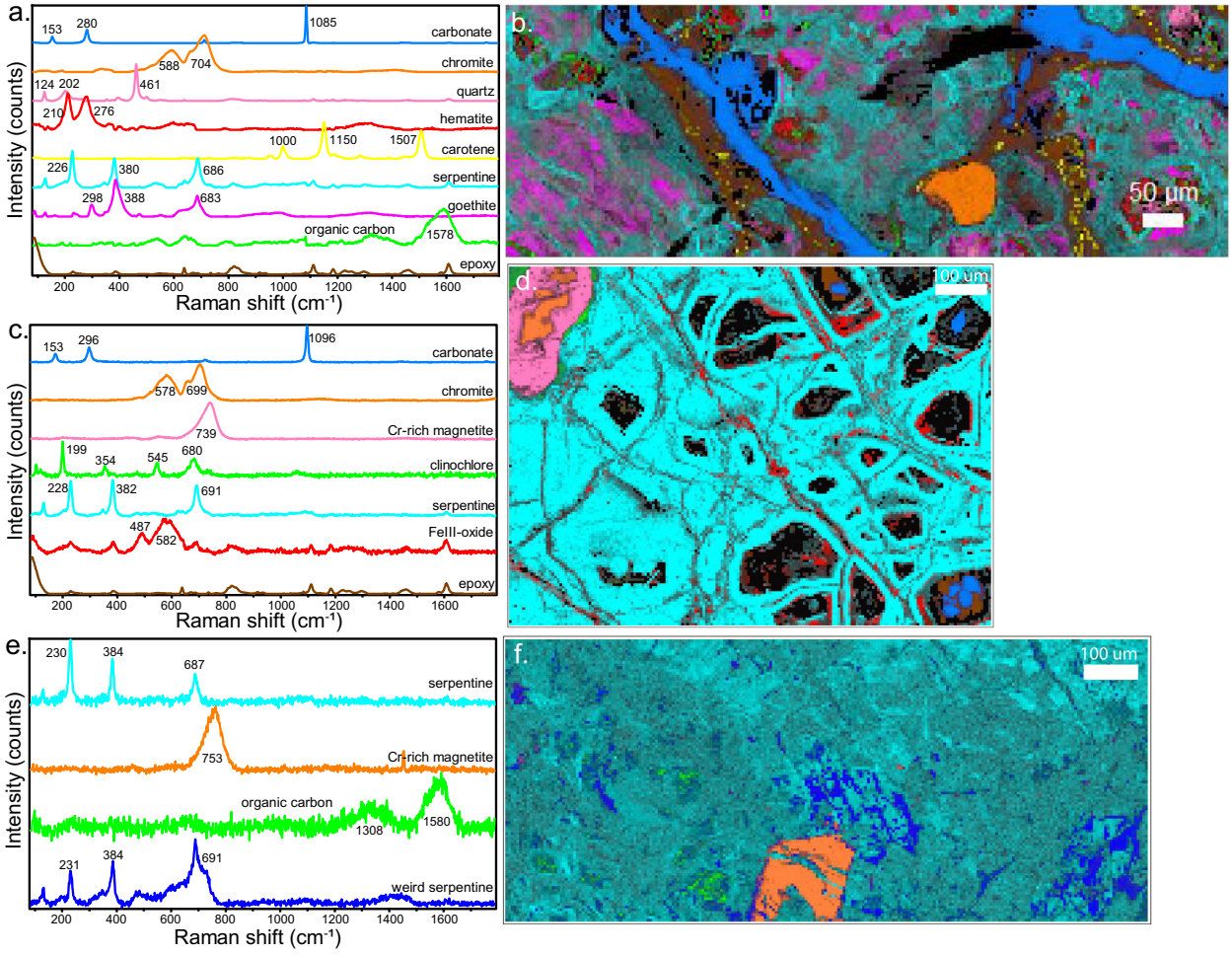

Fig. 6. Raman spectra of the mineral components of highly reacted Oman serpentinites (a) OM08-206D, (c) OM09-129, and (e) OM08-01. A classical least squares fit of the component phases to hyperspectral Raman datasets is used to map the distribution of minerals in each sample (b) OM08-206D, (d) OM09-129, and (f) OM08-01.

tion of Mn, Ni, and Ca (Table 2). Olivine in the dunite OM95-35 has an average composition of $Fo_{90}(Mg_{1.8}Fe_{0.2}SiO_4)$ (Table 2). The average olivine composition of the harzburgite OM94-61, $Fo_{92.12}$, was determined by Hanghoj et al. (2010) and was corroborated by our independent analyses (Table 2). Olivine in the intermediate harzburgite/dunite OM14-05 has an average composition of Fo_{92} (Table 2). These values are similar to those determined in much larger studies by Hanghoj et al. (2010, 27 Oman dunites and harzburgites) and Monnier et al. (2006, 739 olivines in 170 harzburgites and dunites).

The average XFe of pyroxene in these rocks varied from 0.05 to 0.08 (Table 2). Hanghoj et al. (2010) determined that the Fs (ferrosilite $FeSi_2O_6$) content of pyroxene in OM94-61 is 8.17, slightly less than their average harzburgite value (9.09). A single analysis of pyroxene in OM95-35 contained 11 mol% Fs while pyroxene in OM14-05 contained only 5% (Table 2).

Microprobe imaging and analyses of samples OM94-61, OM95-35, OM14-05, -06, and -08 revealed a range of back scatter electron (BSE) signals from darker (less electron dense) to brighter (more electron dense) within the serpentine-rich areas that correspond to variation in the Fe and Si content. Low silica values were interpreted to be due to mixture of serpentine with brucite (e.g. Bach et al., 2006; Bonnemains et al., 2016). An average molar Si/(Mg + Fe) was calculated for each analysis in order to estimate the proportion of brucite mixed with serpentine (Table 2). We considered that

$$\text{molar Si}/(\text{Mg}+\text{Fe})_{\text{serpentine}} \sim 0.67$$

Therefore the molar percentage of brucite was calculated according to

$$1-(\text{molar Si}/\text{Mg}+\text{Fe})_{\text{measured}}/0.67)*100.$$

The Fe(III)-bearing serpentine cronstedtite ($(Fe_2^{2+},Fe^{3+})(SiFe^{3+})O_5(OH)_4$) also has molar $Si/(Mg+Fe)_{serpentine} < 0.67$, similar to mixtures of serpentine and brucite. However, we do not expect significant amount of cronstedtite to occur in the less-altered serpentinites in which brucite is detected. Other phases such as Fe-bearing talc and Fe-sulfides also have molar $Si/(Mg+Fe)_{serpentine} < 0.67$,

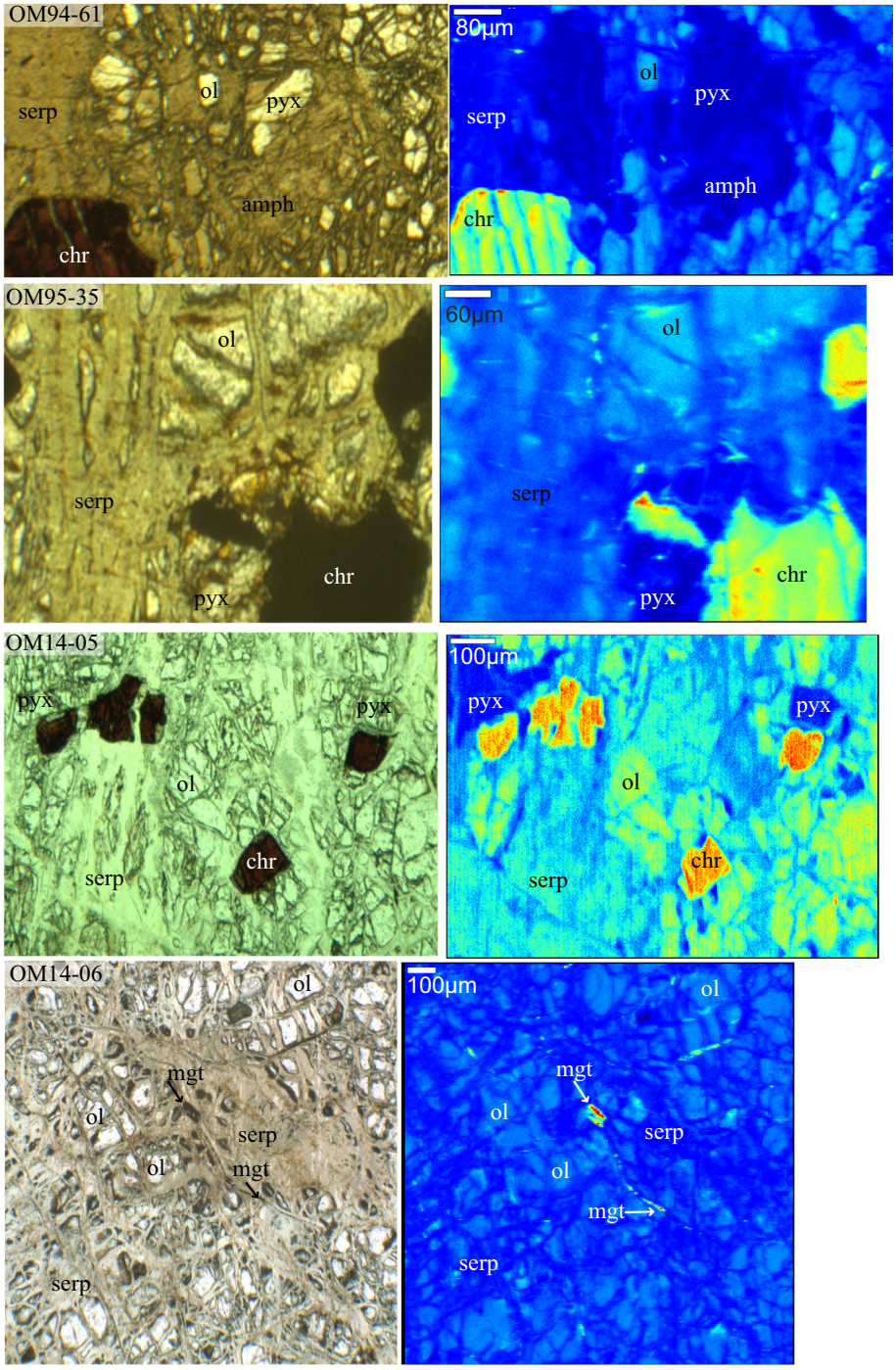

Fig. 7. Synchrotron-radiation based X-ray fluoresence heat maps of iron in the less-altered Oman peridotites with coresponding plane polarized light optical images. The concentration of Fe in the different mineral phases varies from high (red) to low (dark blue). Sample names are given in the upper left corner of the plane polarized light image. ol = olivine, chr = chromite, pyx = pyroxene, mgt = magnetite, serp = serpentine. (For interpretation of the references to colour in this figure legend, the reader is referred to the web version of this article.)

however we do not have evidence for the presence of such phases mixed with serpentine at the microscale. Mixtures with ≤10% brucite are heretofore referred to as serpentine, mixtures with 11%–50% brucite are referred to as serpentine + brucite, mixtures with 50%–89% brucite are referred to as brucite + serpentine, and mixtures with ≥90% brucite are referred to as brucite. In OM95-35, variations in the BSE signal and quantitative WDS analyses revealed a serpentine phase with an average of 3.65 wt% FeO (Table 2); a phase called serpentine + brucite 1 with an average of 11.64 wt% FeO and 43% brucite; and a phase called serpentine + brucite 2 with an average of 7.12 wt%

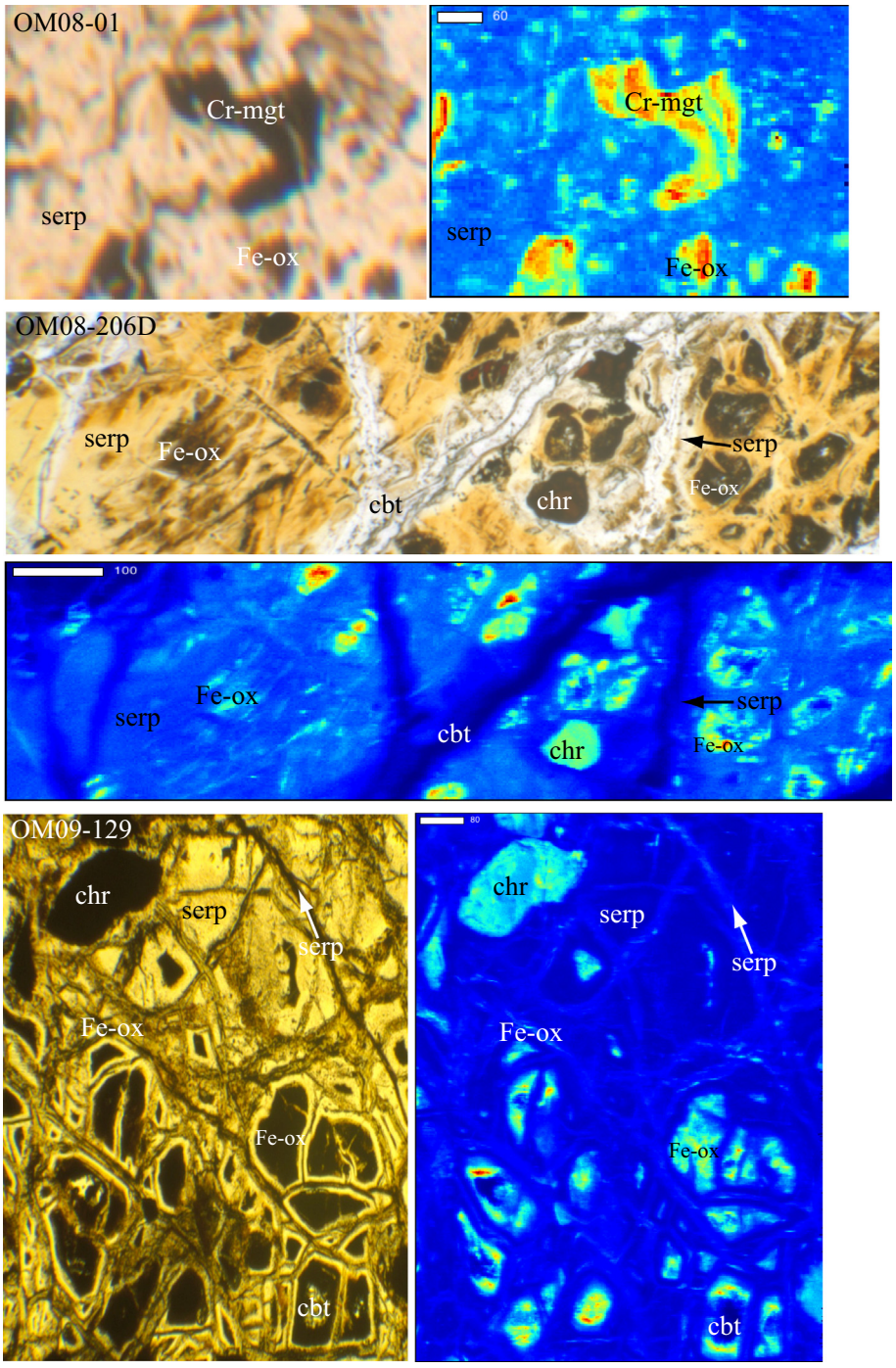

Fig. 8. Synchrotron-radiation based X-ray fluoresence heat maps of iron in highly altered Oman serpentinites with coresponding plane polarized light optical images. The concentration of Fe in the different mineral phases varies from high (red) to low (dark blue). Samples are labeled in the upper left hand corner of the plane polarized light image. ol = olivine, Cr-mgt = chromium-rich magnetite, serp = serpentine, Fe-ox = FeIII-oxides, cbt = carbonate. (For interpretation of the references to colour in this figure legend, the reader is referred to the web version of this article.)

FeO, (essentially equal to the average wt% FeO of the serpentine and serpentine + brucite 1 phases) and 18% brucite (Table 2).

Brucite was detected in OM94-61 where only serpentine with an average of 5.83 wt% FeO was observed (Table 2). Samples OM14-05 and OM14-06 also contained a serpentine phase with 4.88 and 4.32 wt% FeO, respectively (Table 2). Mixtures of serpentine + brucite were also found in samples OM14-05 and OM14-08. Notably, samples OM94-61, OM95-35, OM14-05, -06, and -08 all contain abundant brucite identifiable by higher BSE signals and lower Si contents and higher Fe contents than serpentine

Table 2
Electron microprobe analyses of select Fe-bearing mineral phases in less-altered Oman peridotites.

Sample	OM94-61			OM95-35							OM14-05			
Phase	Ol	Pyx	serp	ol	pyx	chr	mgt	Serp + brc 1	serp	Serp + brc 2	Ol	Pyx	serp	Brc + serp
# of analyses	4	3	11	5	1	2	5	4	3	13	6	5	10	3
Average oxide wt% (± stdev)														
NaO	0	0	nd	nd	nd	nd	nd	nd	nd	nd	0	0.29 (0.07)	nd	nd
MgO	50.76 (0.35)	34.26 (0.14)	36.01 (3.17)	48.89 (0.56)	16.23	9.02 (0.24)	1.70 (0.93)	39.63 (1.98)	39.72 (1.10)	38.83 (1.66)	50.53 (0.42)	17.54 (0.25)	36.78 (1.82)	41.78 (2.35)
Al_2O_3	0	2.27 (0.07)	0.73 (0.82)	0.02 (0.04)	1.94	18.55 (0.40)	1.60 (1.36)	0.01 (0.02)	0.23 (0.18)	0 (0.01)	0	1.46 (0.39)	0.25 (0.26)	0
SiO_2	40.94 (0.51)	55.56 (0.53)	36.99 (2.44)	40.14 (0.18)	50.84	0	0.63 (0.26)	26.26 (2.43)	39.64 (1.38)	34.60 (2.28)	40.92 (0.47)	53.41 (0.99)	36.69 (2.74)	10.57 (5.69)
SO_3	nd	nd	nd	nd	nd	0	0	0.09 (0.04)	0.10 (0.04)	nd	nd	nd	nd	nd
CaO	0.02 (0.02)	0.78 (0.25)	0.13 (0.09)	0.23 (0.10)	25.23	0	0.40 (0.25)	0.09 (0.02)	0.07 (0.02)	0.05 (0.02)	0.02 (0.01)	23.65 (0.64)	0.10 (0.07)	0.30 (0.08)
TiO_2	0	0.01 (0.02)	nd	0	0.73	0.62 (0.01)	0.72 (0.59)	0	0	0	0	0.13 (0.03)	nd	nd
Cr_2O_3	nd	nd	nd	0	0.33	35.87 (0.39)	9.39 (7.67)	0	0	0	nd	nd	nd	nd
MnO	0.10 (0.01)	0.13 (0.02)	0.06 (0.08)	0.18 (0.02)	0	0.66 (0.01)	0.33 (0.27)	0.25 (0)	0.04 (0.03)	0.10 (0.06)	0.12 (0.02)	0.07 (0.04)	0.04 (0.07)	0.68 (0.09)
FeO[a]	7.54 (0.20)	5.04 (0.06)	5.83 (1.18)	10.02 (0.21)	2.10	32.60 (0.56)	82.29 (11.88)	11.64 (0.82)	3.65 (1.14)	7.12 (1.23)	7.50 (0.25)	1.78 (0.10)	4.88 (0.82)	17.50 (1.77)
CoO	nd	nd	nd	nd	nd	0.07 (0.01)	0.10 (0.03)	nd	nd	nd	nd	nd	nd	nd
NiO	nd	nd	nd	0.11 (0.14)	0.07	0.19 (0.01)	0.29 (0.17)	0.28 (0.04)	0.12 (0.12)	nd	nd	nd	nd	nd
ZnO	nd	nd	nd	nd	nd	0.18 (0.01)	0.02 (0.04)	nd	nd	nd	nd	nd	nd	nd
Total	99.38 (0.99)	98.09 (0.65)	79.75 (2.96)	99.58 (0.45)	97.46	97.74 (1.58)	97.46 (0.93)	78.06 (1.96)	83.50 (1.36)	80.72 (4.37)	99.10 (1.07)	98.34 (1.22)	78.71 (3.48)	70.82 (2.41)
XFe[b]	0.08 (0)	0.08 (0)	0.08 (0.02)	0.10 (0)	0.11	NA	NA	0.14 (0.01)	0.05 (0.02)	0.09 (0.01)	0.08 (0)	0.05 (0)	0.07 (0.01)	0.19 (0.02)
Si/(Mg + Fe)	NA	NA	0.63 (0.07)	NA	NA	NA	NA	0.38 (0.05)	0.64 (0.02)	0.55 (0.03)	NA	NA	0.62 (0.05)	0.14 (0.08)
%brc	NA	NA	0.05 (0.08)	NA	NA	NA	NA	0.43 (0.07)	0.05 (0.03)	0.18 (0.05)	NA	NA	0.07 (0.08)	0.79 (0.12)

Sample	OM14-06			OM14-08	
Phase	serp	brc	Unknown	Serp + brc	Brc + serp
# of analyses	6	9	3	5	3
Average oxide wt% (± stdev)					
NaO	nd	nd	nd	nd	nd
MgO	38.78	49.67	47.30	37.90	41.34
	(1.27)	(3.68)	(6.16)	(1.48)	(1.92)
Al_2O_3	0.56	0.07	1.20	0.05	0.02
	(0.51)	(0.03)	(1.64)	(0.05)	(0.03)
SiO_2	37.14	1.19	5.11	35.52	10.75
	(2.48)	(0.75)	(1.91)	(1.64)	(0.81)
SO_3	nd	nd	nd	nd	nd
CaO	nd	nd	nd	0.04	nd
				(0.03)	
TiO_2	nd	nd	nd	nd	nd
Cr_2O_3	nd	nd	nd	nd	nd
MnO	nd	nd	nd	0.10	0.32
				(0.09)	(0.07)
FeO[a]	4.32	15.80	13.52	6.28	18.16
	(1.11)	(2.97)	(0.79)	(0.90)	(1.52)
CoO	nd	nd	nd	nd	nd
NiO	nd	nd	nd	nd	nd
ZnO	nd	nd	nd	nd	nd
Total	80.52	66.71	66.73	79.89	70.73
	(1.69)	(1.91)	(4.16)	(0.85)	(1.27)
XFe[b]	0.06	0.15	0.14	0.08	0.20
	(0.01)	(0.03)	(0.01)	(0.01)	(0.02)
Si/(Mg+Fe)	0.61	0.01	0.06	0.54	0.17
	(0.05)	(0.01)	(0.02)	(0.09)	(0.02)
%brc	0.10	0.98	NA	0.19	0.74
	(0.08)	(0.01)		(0.14)	(0.03)

nd = no data (ol = olivine; pyx = pyroxene; serp = serpentine; chr = chromite; mgt = magnetite; brc = brucite).

[a] Fe_3O_4 for the magnetite analyses.

[b] XFe = molar Fe/(molar Fe + molar Mg).

(Table 2). The MnO content of mixtures in which brucite is the major phase is greater than that of the more serpentine-rich phases (Table 2). Sample OM14-06 was unique because it contained the most pure brucite (98%; average SiO_2 = 1.19 wt%). Quantitative microprobe analyses of the brucite showed the Fe content varies from 11.72 to 20.13 wt% FeO, which is significantly more enriched in FeO than the serpentine from this sample (Table 2). An unidentified phase observed at the interface of olivine and brucite in OM14-06 (Fig. 5f) was also found to contain substantial Fe (average = 13.52 wt% FeO) and a low Si content (Table 2). While these values are similar to those of brucite, Raman spectra of this phase do not match brucite (Fig. 5e).

The Fe-content of the brucite in mixtures was estimated based on the position of the brucite OH stretch peak in the Raman spectrum near 3650 cm^{-1}. The position of this peak shifts to lower wavenumbers with increasing substitution of Fe into brucite (Reynard et al., 2015). An average Fe content of brucite in the mixed Raman spectra was determined by averaging the brucite spectra from many pixels in a representative map area. The centroid of the average brucite peak was calculated and compared to a calibration curve (error ~ 5%) derived from a suite of 20 natural and synthetic brucites (Miller et al., 2017). Using this method, the Fe content of brucite in OM94-61 is estimated to be 12 wt % FeO, in OM95-35 it is 18 wt% FeO (Miller et al., 2017), and in OM14-05 it is 11 wt% FeO.

3.3.3. Fe K-edge XANES insights into Fe oxidation state

Micro-XANES spectroscopy was used to qualitatively interrogate the oxidation state of Fe in serpentine. The serpentine spectra from samples OM94-61, OM95-35, and OM14-06 have more reduced (lower energy) edge and peak positions. Fits to these spectra often include a serpentine spectrum with lower energy edge and peak positions, suggesting that the Fe is more reduced, with minor contributions from more oxidized models including Fe(III)-rich serpentine and Fe(III)-(hydr)oxides. Serpentine spectra from samples OM08-01, OM08-206D, and OM09-129 have higher energy edge and peak positions (Fig. 9) and fits are either dominated by a Fe(III)-oxide spectrum or a Fe(III)-bearing serpentine spectrum with higher energy edge and peak positions suggesting that the Fe is more oxidized (Table 3).

Robust quantification of the Fe^{3+}/Fe_{Total} (e.g. Wilke et al., 2001; Andreani et al., 2013; Munoz, 2013) was not undertaken. However, general differences in the shape, position, and intensity of the pre-edge feature provide further insights into the Fe oxidation state of serpentine. The pre-edge of most serpentines from samples OM94-61, OM95-35, and OM14-06 have a higher intensity feature at lower energy, resulting in a centroid position at ~7113.5 (Fig. 10) and peak areas that range from 0.05 to 0.08 (Table 4). This is in contrast to samples OM08-01, OM08-206D, and OM09-129 that have a centroid position at 7114.5 eV (Fig. 10) and larger peak areas (0.09–0.17) (Table 4). These observations suggest a higher oxidation state and the presence of tetrahedrally coordinated Fe(III) in samples OM08-01, OM08-206D, and OM09-129, consistent with observations from fits to the full μXANES spectra and bulk XANES data.

4. DISCUSSION

4.1. Diverse assemblage of Fe(II) reservoirs in less-altered Oman peridotites

To track dynamic Fe transformations and assess the potential for H_2 production in the Samail ophiolite, it is important to document not only the presence and distribution of Fe(II)-bearing primary minerals but also potentially

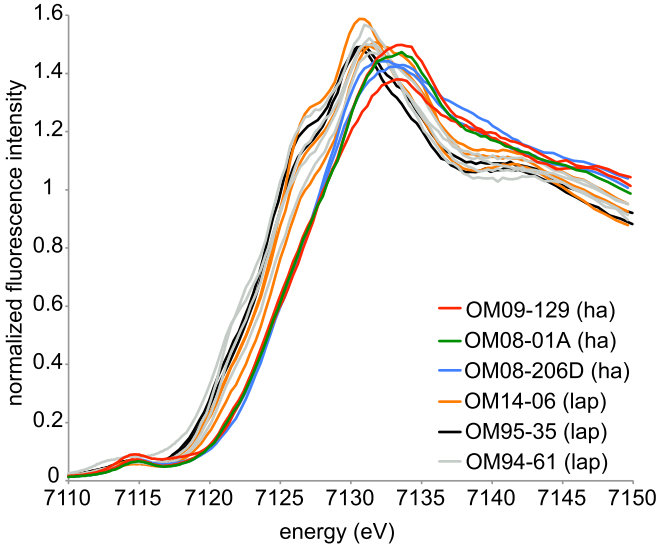

Fig. 9. Fe K-edge μXANES spectra of serpentine or serpentine-bearing materials within Oman peridotites. The edge and peak positions of spectra from the less altered peridotites are at lower energies than those of spectra from the highly altered rocks. These structural differences suggest Fe is more oxidized in the highly altered rocks. Multiple spectra were collected from each sample and are labeled with the same color. The letters after the sample name indicate if the sample is a less altered (lap) or highly altered (ha) peridotite. (For interpretation of the references to colour in this figure legend, the reader is referred to the web version of this article.)

Table 3
Non-negative least square fits of Fe model compounds to representative serpentine XANES spectra from Oman serpentinites. The R-factor (Newville, 1998) was less than $3.7e^{-4}$ for all fits. The energy shift required for fitting ranged from −0.28 to 0.22 eV for all spectra.

Sample spectrum/Fe model compound	Normalized proportion[a]
OM94-61-8	
Fe-phyllosilicate	0.48
Fe(III)-serpentine	0.35
Fe(III)-oxide	0.17
OM94-61-11	
Fe-phyllosilicate	0.76
Fe(III)-oxide	0.13
Fe-carbonate	0.11
OM94-61-17	
Fe(II)-serpentine	0.69
Magnetite	0.31
OM94-61-18	
Fe(II)-serpentine	0.42
Chromite	0.33
Magnetite	0.25
OM95-35-4	
Fe(II)-serpentine	0.65
Magnetite	0.35
OM95-35-5	
Fe(II)-serpentine	0.53
Fe-phyllosilicate	0.47
OM14-06-7	
Fe(III)-oxide	0.50
Fe(II)-serpentine	0.50
OM14-06-8	
Fe(II)-serpentine	0.73
Fe-phyllosilicate	0.27
OM14-06-16	
Fe(II)-serpentine	0.60
Fe(III)-serpentine	0.33
Fe(III)-oxide	0.07
OM08-01-1	
Fe(III)-serpentine	0.55
Fe-phyllosilicates	0.45
OM08-206D-4	
Fe(III)-oxides	0.69
Fe(II)-serpentine	0.16
Fe-phyllosilicates	0.75
OM08-206D-7	
Fe(III)-oxides	0.62
Fe(III)-serpentine	0.25
Fe(II)-serpentine	0.13
OM09-129-2	
Fe(III)-oxide	0.68
Fe(III)-serpentine	0.19
Magnetite	0.13
OM09-129-13	
Fe(III)-serpentine	0.55
Fe-phyllosilicates	0.23
Fe(III)-oxide	0.22

[a] Note: Identification of phases that occur close to, or below, ~10% of the Fe fluorescence, is uncertain due to the quantitative detection limit of the technique as determined from empirical mixtures (O'Day et al., 2004; Ostergren et al., 1999).

reactive, Fe(II)-bearing secondary phases. We propose that within our suite of samples, OM95-35 represents the least-altered end-member because it possesses the most relict olivine and reduced iron character. Yet, this rock (as well as samples OM94-61, OM14-05, -06, -07, -08, and -10) also possesses Fe(II)-bearing secondary phases such as serpentine and brucite, thus there still remains significant potential for further Fe oxidation such as might occur during modern day low-temperature reaction.

We do not know the timing or the environment of formation of the Fe(II)-bearing secondary phases in the less-altered rocks. Other researchers have suggested that serpentinization may have occurred in a marine environment during obduction of the ophiolite (e.g. Neal and Stanger, 1985; Bosch et al., 2004; Kelemen and Matter, 2008; Boudier et al., 2010; Streit et al., 2012; Bonnemains et al., 2016) at temperatures between 180 and 500 °C (Neal and Stanger, 1985). However, it is difficult to know the maximum extent of alteration during obduction and distinguish it from alteration that occurred after emplacement of the ophiolite. Despite these complexities, the Oman serpentinites likely represent an integrated history of reaction at low temperature thus they are a best example of low temperature serpentinization for studying Fe transformations regardless of the timing and environment of alteration.

4.1.1. Fe(II)-bearing serpentine

A significant fraction of Fe in serpentine in less-altered peridotites appears to be present as Fe(II) (see Section 3.3.3, Fig. 10, Table 3) and calculations of whole rock Fe^{3+}/Fe_{Total} ratios from less-altered peridotites (~0.4–0.5) are consistent with this observation. This is also consistent with observations of Fe(II)-rich serpentine during initial stages of serpentinization documented for experimental (e.g. Marcaillou et al., 2011) and natural systems (e.g. Andreani et al., 2013). In the Oman system, serpentine can be considered a reservoir of iron that may be transformed during low temperature water-rock reactions. The serpentine phases analyzed here have XFe from 0.05 to 0.09 with an average of 0.07. The high XFe of serpentine values reported here are consistent with results from other low temperature, magnetite-poor serpentinites (XFe ~ 0.05–0.1, Klein et al., 2014; XFe ~ 0.06, Bonnemains et al., 2016). Other previous work on the petrology and geochemistry of less-altered Oman peridotites (Godard et al., 2000; Monnier et al., 2006; Hanghoj et al., 2010) did not include quantitative chemical analyses of serpentine so direct comparisons cannot be made. A more recent study by Bonnemains et al. (2016) reported an average FeO content ~6 wt% for mesh texture serpentine, attributed to the low temperature of reaction resulting in the absence of magnetite in four samples from Oman. Our values are consistent with the FeO content of serpentine in subsurface Oman rocks ~6–8 wt% (Miller et al., 2016). Our analyses of serpentine in less-altered peridotites, while limited in number, show a higher, more narrow range of XFe values than the broad compilation of values reported by Evans et al. (2009) (n ~ 480 analyses, XFe ~ 0.02–0.08 with values of 0.03–0.04 most commonly reported). The Fe content of serpentine in the less-altered peridotites analyzed in this study (average XFe = 0.07) is less than the average XFe of relict olivine and pyroxene in Oman serpentinites (~0.09, Monnier et al., 2006; Hanghoj et al., 2010). Thus,

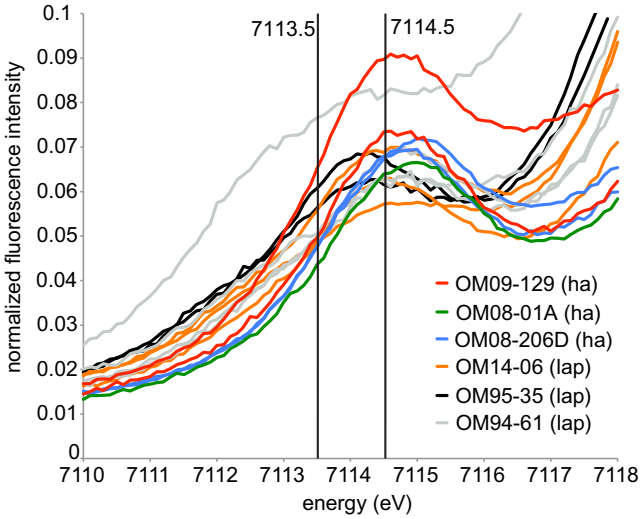

Fig. 10. Plot of the pre-edge feature of Fe K-edge μXANES of serpentine and serpentine-bearing materials from Oman peridotites. The average centroid position of spectra from the less altered peridotites (lap) is 7113.8 eV and from highly altered rocks (ha) is 7114.5 eV. Lines indicating the positions of 7113.5 and 7114.5 eV are labeled on the plot for reference. While this data was not calibrated to Fe(II)/Fe(III) standards it does suggest that Fe in serpentine in the highly altered rocks is more oxidized than in the less altered peridotites.

Table 4
Pre-edge peak centroid positions and areas calculated from representative serpentine XANES spectra of Oman serpentinites. Spectra are listed from smallest to largest peak area.

Spectrum	Centroid	Area
OM14-06-8	7113.81	0.052
OM94-61-11	7113.75	0.060
OM95-35-5	7113.42	0.067
OM94-61-17	7113.99	0.075
OM95-35-4	7113.62	0.078
OM14-06-16	7114.06	0.078
OM14-06-7	7113.94	0.081
OM94-61-18	7113.12	0.084
OM94-61-8	7114.13	0.085
OM08-01-1	7114.53	0.090
OM08-206D-4	7114.58	0.095
OM08-206D-7	7114.43	0.100
OM09-129-13	7114.38	0.105
OM09-129-2	7114.57	0.171

the 'missing' iron must then be partitioned into a Fe-bearing secondary phase(s) other than serpentine (e.g. Oufi et al., 2002; Evans, 2008).

4.1.2. Fe content of brucite

We have demonstrated that in the less-altered peridotites much of what may be considered serpentine at first glance is, in fact, serpentine mixed with brucite. Intergrowth of brucite and lizardite has been observed in abyssal serpentinites (e.g. Oufi et al., 2002; Bach et al., 2004, 2006; Klein et al., 2009), in serpentine mud volcanoes (D'Antonio and Kristensen, 2004; Kahl et al., 2015), orogenic serpentinites (e.g. Hostetler et al., 1966), and ophiolite complexes (e.g. Katayama et al., 2010; Frost et al., 2013; Schwarzenbach et al., 2016). However, the brucite content of partially serpentinized peridotites in Oman has previously been thought to be low (Neal and Stanger, 1985). Though, the intergrowth of serpentine and brucite was previously observed by TEM in a single Oman harzburgite (Baronnet and Boudier, 2001) and has recently been documented in surface (Bonnemains et al., 2016) and subsurface Oman rocks (Miller et al., 2016).

Our work documented the significant incorporation of Fe into relatively pure brucite in OM14-06, one of the less-altered Oman peridotites, using quantitative electron microprobe analyses (XFe = 0.15, Table 2). The partitioning of Fe into brucite, particularly during low temperature reactions, has been demonstrated experimentally and theoretically (Moody, 1976a,b; Sleep et al., 2004; Seyfried et al., 2007; McCollom and Bach, 2009; Klein et al., 2009) and observed in natural systems (Hostetler et al., 1966; Page, 1967; Evans and Trommsdorf, 1972; Moody, 1976a; D'Antonio and Kristensen, 2004; Bach et al., 2006; Klein et al., 2014). Our value falls within the range of Fe contents measured in brucite formed experimentally (0–30% Moody, 1976a; Seyfried et al., 2007). In addition, our value is approximately twice that of the co-existing serpentine and falls slightly off the equilibrium distribution line proposed by Evans and Trommsdorf (1972). The production of brucite with an iron content greater than co-existing serpentine has also been observed in natural (e.g. Hostetler et al., 1966; Page, 1967; Evans and Trommsdorf, 1972; Moody 1976b; Oufi et al., 2002; D'Antonio and Kristensen, 2004; Bach et al., 2006) and experimental samples (Okamoto et al., 2011; Malvoisin et al., 2012b; Lafay et al., 2012; Ogasawara et al., 2013; McCollom et al., 2016) and is predicted by thermodynamic models (McCollom and Bach, 2009; Klein et al., 2009). The XFe of brucite + serpentine mixtures ranges from 0.08 to 0.2 (Table 2). For samples in which it was possible to estimate the Fe content of the

brucite in the serpentine + brucite mixtures, the estimated wt% FeO is higher in brucite than in corresponding serpentine (Table 2). However, direct comparisons of molar XFe of brucite and serpentine in these samples are not possible because microprobe data could not be obtained from each phase independently. Additionally, the observation of Fe-bearing brucite is notable because the production and subsequent reaction of Fe-bearing brucite to form carbonates, Fe(III)-bearing serpentines, and magnetite has been proposed to occur in other serpentinizing systems (e.g. Toft et al., 1990; Bach et al., 2006; Frost et al., 2013) and has been observed in mine tailings and experiments (Harrison et al., 2013, 2015).

4.2. Highly altered rocks possess a more limited assemblage of minerals

We have identified a subset of samples (OM08-01, OM08-206A/D, OM09-129 and OM14-11) that are the most highly altered end-members of those studied here. These highly altered rocks possess a diverse mineral assemblage but contain fewer unique phases than the less-altered peridotites. No relict olivine remains in these samples, though relict pyroxenes are present in greater abundance than in the less-altered peridotites (Table 1; Fig. 4). Chromite is less abundant and often appears to be more extensively fractured and altered to Cr-rich magnetite and chlorite than in the less-altered peridotites. This is evidence of continued alteration of chromites during low temperature serpentinization.

Serpentine, while a major phase in the highly altered rocks, does not appear to be more abundant than in the less-altered peridotites. However, if carbonate is removed from consideration because it is likely to have precipitated out of a fluid rather than representing direct, in place alteration of peridotite, the average abundance of serpentine in highly altered samples than represents a 20% increase over the less-altered samples. As such, serpentine may be a larger reservoir of Fe in the highly altered rocks than in the less altered rocks. Hematite and goethite are intermixed with serpentine in some samples whereas magnetite is generally absent from the highly altered rocks (except where localized around chromian spinels). These observations are consistent with the results of Streit et al. (2012) who found that hematite is more common than magnetite in these highly altered rocks. This is likely because carbonated peridotites form at high oxygen fugacities, conditions under which hematite is stable (c.f. Eckstrand, 1975; Frost, 1985). Carbonate is the second most abundant alteration phase, after serpentine, though we determined that it is Fe-poor.

4.2.1. Serpentine in highly altered rocks is not more Fe-rich than in the less-altered peridotites

There is significant incorporation of Fe into serpentine in highly reacted Oman serpentinites as documented by Streit et al. (2012). Notably, quartz-bearing serpentinites (e.g. OM08-206A/D) have significantly higher Fe in serpentine than serpentine in quartz-free serpentinites (e.g. OM08-01, OM09-12) (Streit et al., 2012). The average wt% FeO of serpentine in the quartz-bearing serpentinites investigated in this current study is 7.65 and 7.42 in OM08-206A and OM08-206D, respectively (Streit et al., 2012). The average wt% FeO of serpentine in the quartz-free serpentinites investigated in this current study is 6.04 in OM08-01 and 3.69 in OM09-129 (Streit et al., 2012). The average wt% FeO values for serpentine in the quartz-free highly reacted rocks are similar to the average wt% FeO values for serpentine in the less-altered peridotites (Table 2; 3.65–5.83 wt% FeO). Thus, in general, there is not a significant increase in the Fe content of serpentine between the less-altered peridotites and the 'average' highly altered peridotites.

The FeO content of serpentine in less and more altered rocks is similar, indicating that significant enrichment or depletion of Fe in serpentine did not occur during the transition from less-altered peridotites to highly reacted rocks. This is in contrast to observations from other systems where serpentine produced during early stages of reaction is more Fe-rich than serpentine produced during later stages of reaction (e.g. Toft et al., 1990; Oufi et al., 2002; Marcaillou et al., 2011; Andreani et al., 2013). In these systems, the authors propose that the decrease in Fe in serpentine is due to changing conditions to favor Mg-rich serpentine and Fe partitioned into magnetite. More recent works have attributed the coupled production of Mg-rich serpentine and magnetite (vs. Fe-rich serpentine without magnetite) to serpentinization at temperatures > 200 °C (Klein et al., 2014; Bonnemains et al., 2016). In the highly altered rocks in this study, serpentine does not appear to become more Mg-rich and magnetite is not prevalent. Our observation of a steady Fe-content in serpentine is, however, consistent with that of Bach et al. (2006) who found that the XFe of serpentine formed initially from reaction of olivine is the same XFe as that of serpentine formed later from the reaction of Fe-rich brucite with silica.

4.2.2. Fe in serpentine appears more oxidized in highly altered rocks

Though the total Fe content of serpentine in the highly altered rocks does not appear to have changed, the iron is more oxidized and some may be in tetrahedral coordination (e.g. Marcaillou et al., 2011; Andreani et al., 2013; Miller et al., 2016). Streit et al. (2012) suggested that Fe(III) substitutes into serpentine in these Oman rocks and there are observations of Fe(III) incorporation into serpentine in subsurface Oman rocks (Miller et al., 2016). Those samples that appear to have more oxidized serpentine also have whole rock Fe^{3+}/Fe_{Total} ratios of ~0.9. The presence of larger amounts of Fe(III) in serpentine in more extensively serpentinized rocks and in veins representative of later stages of reaction is consistent with observations from other natural (Whittaker and Wicks, 1970; O'Hanley and Dyar, 1993; Evans, 2008; Evans et al., 2009; Andreani et al., 2013; Miyoshi et al., 2014; Beard and Frost, 2016) and experimental systems (Seyfried et al., 2007; Marcaillou et al., 2011).

The increase in oxidized Fe in the highly altered rocks may be due to: 1) more oxidized Fe in serpentine in the

highly altered rocks that is partly incorporated into tetrahedral sites or 2) the mixing of serpentine with Fe(III)-oxides on the nanoscale, which does not necessitate a change in the oxidation state of Fe in serpentine. The contribution of Fe (III) from oxide phases could also account for the more tetrahedral appearance of the iron spectra. Streit et al. (2012) reported the occurrence of a sub-micron-sized Fe-rich phase mixed with quartz in samples OM08-206A/D but Fe(III)-oxides mixed with serpentine were not reported. It is not possible to address this problem with EMP analyses because of the scale of possible intermixing of serpentine with another Fe-rich phase versus the scale of the analyses.

4.2.3. Fe-bearing brucite is absent from highly reacted rocks

As Oman serpentinites become highly altered, there is the notable disappearance of brucite. Streit et al. (2012) were the first to note the absence of brucite (using EMP) in samples OM08-01, OM08-206A/D, and OM09-129 and suggested that brucite broke down to form magnesium carbonates during reaction with CO_2. Similarly, Neal and Stanger (1985) propose that brucite formed during alteration of olivine in Oman rocks is redissolved upon contact with bicarbonate rich waters associated with complete serpentinization, as observed in mine tailings and experiments by Harrison et al. (2013, 2015). It is certainly possible that the Mg-carbonates observed in these rocks formed from the breakdown of brucite. However, this does not explain the fate of the Fe that was held in brucite as the carbonates are Fe-poor. Some Fe may be accounted for by incorporation into serpentine, as discussed in Section 4.2. Considering that magnetite is not detected (see Section 4.2) and serpentine in the 'average' highly altered rocks does not have a significantly higher Fe-content than serpentine in the less-altered peridotites (see Section 4.2.1), it is likely that the Fe(III)-(hydr)oxides that we see in the highly altered rocks accommodate some of the iron released during the breakdown of brucite.

Whole rock analyses revealed that the highly reacted rocks are Fe-poor as compared to the less-altered peridotites (average %Fe 4.6 vs. 6.4). This observation is consistent with, but more pronounced than, data from the Pindos ophiolite where rocks with serpentinization degree > 50% have an average %Fe = 8.54 while less serpentinized rocks have an average %Fe = 9.27 (data from Bonnemains et al., 2016). One possible explanation of the inconsistency in the total amount of Fe between less and more altered serpentinites may be the breakdown of Fe-rich brucite leading to Fe mobilization vs. in-situ reprecipitation. As aqueous Fe(II) was detected in hyperalkaline fluids from Oman boreholes (Rempfert et al., 2017), this may be a plausible explanation. Iron mobilization may be due to interaction with a CO_2-bearing fluid (e.g. Fujii et al., 2014; Debret et al., 2016) such as would be necessary to form the highly reacted and carbonated Oman rocks. Interestingly, magnetite-rich rocks do occur at discrete locations in Oman and can be found in outcrop as well as at specific depths within borehole wells (c.f. Miller et al., 2016). The occurrence of magnetite-rich rocks perhaps represent the fate of the mobilized Fe and thus may record pulses of Fe mobilization occurring during serpentinization.

4.3. Possible Fe-oxidation pathways during water/rock reaction

4.3.1. Partial serpentinization of Oman peridotites produces Fe-bearing serpentine and brucite

Using microscale geochemical techniques we detected Fe-bearing brucite, often intimately intermixed with serpentine. We consider these phases to be the result of an earlier stage of serpentinization, perhaps during alteration in a marine environment (e.g. Neal and Stanger, 1985; Bosch et al., 2004; Kelemen and Matter, 2008; Boudier et al., 2010; Streit et al., 2012). Neal and Stanger (1985) suggest early formed serpentine is characterized by high(er) concentrations of Mn (~0.15 wt% MnO) and Fe (~8–12 wt% FeO) and lower Si and Mg contents than serpentine formed during later, lower temperature serpentinization. These authors note the scarcity of brucite in Oman rocks despite the prolific olivine hydration that they believe should have produced extensive brucite. They propose that brucite formed but was altered or removed during subsequent reaction. We propose that instead brucite may actually be intimately intermixed with serpentine and difficult to detect. This is supported by trends in Mn, Fe, and Si content reported by Neal and Stanger (1985) which are consistent with those of the serpentine + brucite mixtures measured in this work (Table 2). In other recent work on Oman serpentinites, the authors postulated that low wt% SiO_2 values of serpentine may be due to intergrowth with brucite (Bonnemains et al., 2016).

Considering that sample OM95-35 is the least-altered end-member peridotite studied here, we use this rock to represent an example of this first stage of serpentinization. Reaction 1 then represents a possible reaction pathway experienced by OM95-35 during the first stage of serpentinization. Considering the nature of these reactions and the observation that some oxidized iron is incorporated into serpentine, the production of H_2 is included in Reaction 1.

$$\text{olivine} \pm \text{pyroxene} + H_2O \rightarrow \text{Fe(II)} \gg \text{Fe(III)-serpentine} + \text{Fe(II)-brucite} \pm \text{Fe-poor amphibole/talc} + \text{trace magnetite} \pm SiO_2(aq) + H_2 \quad \text{(R1)}$$

This reaction is generally consistent with the mechanisms proposed by Neal and Stanger (1985) and Bach and Klein (2009) as well as Klein et al. (2014) and Bonnemains et al. (2016). In contrast, Streit et al. (2012) postulated that the earlier, higher temperature stage of serpentinization may have formed Fe-poor serpentine plus magnetite. While there are certainly serpentinites from the Samail ophiolite that have abundant magnetite (e.g. Miller et al., 2016), those were not studied here. Instead, we have included magnetite as only a trace product in

Reaction 2 because in our less-altered samples it is relatively rare and it does not seem likely to have been the main reservoir of oxidized Fe produced during the first stage of serpentinization. The absence of magnetite in early stages of serpentinization is consistent with observations from Oman by other researchers (e.g. Bonnemains et al., 2016) and observations from other serpentinizing systems (e.g. Oufi et al., 2002; Bach et al., 2006; Beard et al., 2009; Katayama et al., 2010; Frost et al., 2013; Klein et al., 2014; Schwarzenbach et al., 2016). The absence of magnetite has been interpreted as evidence for serpentinization occurring at low temperatures (<200 °C) (e.g. Seyfried et al., 2007; Evans, 2008; Klein et al., 2009; Malvoisin et al., 2012a,b; Klein et al., 2014; Bonnemains et al., 2016). However, because there are examples of magnetite-rich Oman serpentinites, that appear to form in specific hydrologic zones through reactions not yet constrained, it is difficult to infer low temperatures of reaction from the absence of magnetite.

In addition to alteration of the primary silicates during this first stage of serpentinization, there is evidence for the partial alteration of primary chromites to magnetite (Reaction 2).

$$\text{chromite} + H_2O \rightarrow \text{Cr-magnetite} + Cr_{(aq)} \pm H_2 \quad \text{(R2)}$$

A key point is that this first stage of the reaction history resulted in only partially serpentinized peridotites. As such, relict Fe(II)-bearing primary phases as well as Fe(II)-bearing secondary phases that were produced including serpentine, brucite, and magnetite (see reactions above) were available for oxidation during subsequent lower temperature serpentinization in Oman.

4.3.2. Low temperature alteration of less-altered Oman peridotites

Four main mineralogical changes are inferred for the transition from the partially serpentinized, less-altered peridotites to the highly reacted serpentinites in Oman. Using OM95-35 as the least altered representative and OM09-129 as the highly altered representative, these transformations are 1) complete loss of olivine, 2) the disappearance of Fe(II)-bearing brucite, 3) a higher oxidized Fe content of serpentine, and 4) the precipitation of Fe-poor carbonates. However, it is important to note that we represent only a single possible initial composition and a single possible product composition. As the Oman ophiolite is dominated by harzburgite, with less abundant lenses of dunite (Boudier and Coleman, 1981; Godard et al., 2000; Monnier et al., 2006; Hanghoj et al., 2010), we may be comparing a less-altered dunite to a highly altered harzburgite. Alteration of harzburgite should result in the production of more serpentine because of its higher Si content. However, in this work we are examining the overall effect of low temperature alteration and it is difficult to assess the original protoliths of the highly altered rocks. It is likely that the reaction pathway consisted of many, complex steps some of which may be represented by the less-altered but more oxidized samples studied here (e.g. OM14-05, -07, -08, and -10).

It is important to note that we do not know the composition of the fluid that reacted with the less-altered peridotites. There are three main fluid compositions observed in Oman today, 1) meteoric water; 2) Type I Mg^{2+}/HCO_3^- waters that result from the reaction of meteoric water with peridotite in contact with the atmosphere; and 3) Type II Ca^{2+}/OH^- waters that result from the continued reaction of Type I waters with peridotite at depths where communication with the atmosphere does not occur (e.g. Barnes and O'Neill, 1969; Barnes et al., 1978; Neal and Stanger, 1985; Dewandel et al., 2005; Kelemen and Matter, 2008; Paukert et al., 2012). Type I waters exist both in open systems in contact with the atmosphere and in closed systems with no contact with the atmosphere. Considering that the rocks studied here were sampled from the surface of the ophiolite and were likely to have been sourced from the shallow aquifer, they would have interacted with Mg^{2+}-rich, moderate pH (~8), high Eh (~200 mV), waters known to contain nitrate (NO_3^-) (Dewandel et al., 2005; Miller et al., 2016). Therefore, Fe could have been oxidized in the presence of nitrate or oxygen as the oxidant. Continued alteration under anoxic, reducing conditions in the absence of these oxidants is also a possibility. However, truly assessing these possibilities is difficult because there are no constraints on the water-rock ratios or the residence time of our samples.

Regardless of the reacting fluid chemistry, we propose that during low temperature alteration, relict olivine and pyroxene and Fe(II)-brucite reacted to form Fe(II)/(III) serpentine, Fe-poor carbonate, and Fe(III)-oxides (Reaction 3). The reaction of pyroxenes would have released SiO_2 to solution so this is included as a reactant. Presumably, reduced Fe in brucite was oxidized and incorporated into Fe(III)-oxides. Since it is not possible to constrain the possible transformation of serpentine, both the production of a serpentine with a greater oxidized Fe content and the production of Fe(III)-oxides are represented in the reaction below.

$$\begin{aligned}&\text{olivine} + \text{pyroxene} + \text{Fe(II)} \gg \text{Fe(III)-serpentine} + \text{Fe(II)-brucite} + H_2O + CO_2 + SiO_{2(aq)} \\ &\quad \rightarrow \text{relict pyroxene} + \text{Fe(III)} \gg \text{Fe(II)-serpentine} + \text{carbonate} + \text{Fe(III)-oxides} \pm \text{quartz} \pm H_2 \quad \text{(R3)}\end{aligned}$$

Chromites in the less-altered peridotites are partially altered to magnetite and there is significant evidence that they underwent further alteration during subsequent low temperature serpentinization, perhaps by a process such as that represented by Reaction 4.

$$\begin{aligned}&\text{chromite} + \text{magnetite} + H_2O \pm SiO_{2(aq)} \\ &\quad \rightarrow \text{Cr-magnetite} \pm \text{clinochlore} \pm H_2 \quad \text{(R4)}\end{aligned}$$

4.4. The potential for H_2 production during low temperature serpentinization

There are numerous mechanisms by which H_2 could have been generated during low temperature water-rock reactions in the Samail ophiolite if the reactions occurred under anoxic, reducing conditions. Considering the significant proportion of Fe-bearing relict olivine present in the less-altered peridotites and the absence of olivine from the highly altered rocks, alteration and hydration of olivine could have played an important role in long-term H_2 generation. However, olivine dissolution at near-surface temperatures is kinetically slow and as such affects the rate of solubilization and release of Fe(II), the key component for H_2 production. At low temperatures, the question remains if oxidation of Fe(II) released from primary minerals will occur in solution or if it may need to be promoted by interfacial electron transfer across the surface of conductive Fe(II)-bearing spinel (e.g. chromite) minerals (Mayhew et al., 2013). A third possible mechanisms is the oxidation of structural Fe(II) in primary spinel phases (Mayhew et al., 2013). Such a process would result in the formation of rims of magnetite around chromite as observed in Oman rocks in this work and by Streit et al. (2012). In contrast to Fe(II) in primary olivine and spinels, there is a relatively small proportion of relict pyroxene that is not particularly Fe-rich in the less-altered peridotites. Additionally, some of this pyroxene remains in the highly altered rocks; thus it is unlikely to have been a significant source of Fe(II) for H_2 production.

Hydrogen may have been generated from the reaction of Fe(II)-bearing secondary phases present in the less-altered peridotites. Serpentine in the less-altered peridotites contains Fe(II) and may act as a reactive phase, with potential oxidation of this iron resulting in H_2 generation, during low temperature serpentinization in the subsurface of Oman. Modeling of water-rock reactions in which Fe(II)-bearing serpentine and brucite were reactants predicted formation of magnetite and Mg-serpentine coupled with H_2 production (Sleep et al., 2004). The transformation of Fe-rich to Mg-rich serpentine has also been inferred from study of naturally serpentinized samples that show higher Fe contents of serpentine (XFe $\sim$ 0.1) in rocks <75% serpentinized and lower Fe contents of serpentine (XFe = 0.03–0.05) in rocks >75% serpentinized (Oufi et al., 2002; Evans, 2008; Andreani et al., 2013). Thus, under suitable reaction conditions, the oxidation of Fe associated with serpentine could have resulted in high amounts of H_2 production. This mechanism of H_2 production during low temperature serpentinization in Oman is consistent with that recently proposed by Miller et al. (2016). Iron bearing brucite present in the less-altered peridotites from Oman may also act as a reactive phase. By definition, the majority of Fe in brucite is Fe(II), thus, the consumption of brucite (e.g. Toft et al., 1990; Bach et al., 2004) and oxidation of Fe could be a potentially important mechanism of H_2 generation during low temperature serpentinization in Oman, as recently suggested for Oman subsurface rocks by Miller et al. (2016).

The mineral products capable of accommodating Fe(III) and thus H_2 production are also not well constrained at low temperatures. From $\sim$150 to 300 °C, magnetite is often the main Fe(III)-bearing product phase (e.g. McCollom and Bach, 2009). But, in both the partially serpentinized, less-altered peridotites and highly reacted rocks studied here, magnetite is a rarity. The absence of magnetite does not preclude H_2 production. Previous experimental and equilibrium thermodynamic modeling work has shown H_2 production in the absence of magnetite (Seyfried et al., 2007; Marcaillou et al., 2011; Andreani et al., 2013; Klein et al., 2013). In these cases, oxidation of Fe(II) to form Fe(III)-bearing serpentine was thought to accommodate H_2 production. Recently, kinetic-thermodynamic models of peridotite-seawater reactions have demonstrated significant H_2 production associated with precipitation of other Fe (III)-oxides, including goethite and hematite, during low temperature serpentinization (Bach, 2016). However, as the reacting fluid composition and the oxygen fugacity in this system are not constrained, it is possible that the conditions precluded H_2 production.

5. CONCLUSIONS

Unraveling the mechanisms and pathways of low temperature serpentinization is challenging. There are often several stages of reaction that occur over millions of years of water-rock reaction, and the temperatures of reaction and fluid compositions may be variable in time and space. It is difficult to acquire samples representative of various stages of alteration under identical conditions, and detailed microscale techniques are time-consuming and complex. Yet, these processes can directly affect the development of microbial energy sources and habitats, and carbon cycling and sequestration within the (ultra)mafic ocean crust. Rocks of the Samail ophiolite in the Sultanate of Oman, currently undergoing low temperature alteration and hydration, serve as an easily accessible case study of these processes.

In this study, we have undertaken a detailed, microscale mineralogical and geochemical analysis of partially and completely serpentinized peridotites of the Samail ophiolite to assess the mineralogy and iron content and oxidation state of mineral reactants and products. We show that the partially serpentinized rocks, which may then undergo further low temperature alteration, possess a variety of Fe(II)-bearing relict primary as well as secondary minerals that may act as reactive phases during low temperature alteration. Primary iron-bearing olivine, pyroxene, and chromite remain as relict phases. Serpentine in the less-altered peridotites is iron-rich and variably intergrown with iron-bearing brucite on the microscale. In contrast, in the completely serpentinized rocks, olivine has been completely reacted and chromites have been extensively altered to magnetite and/or chlorite. On the bulk scale, iron in the completely serpentinized rocks is more oxidized than iron in the partially serpentinized rocks. Iron in serpentine appears more highly oxidized than iron in serpentine in the less-altered peridotites, Fe-bearing brucite is no longer present in highly altered samples, and Fe(III)-oxides are detected. The notable mineralogical and chemical differences between the less-altered peridotites and the completely reacted

peridotites require extensive oxidation of iron. In the absence of oxygen or nitrate, the mechanisms of alteration of the less-altered peridotites to the completely serpentinized rocks certainly have the potential to generate H_2 such as that measured in hyperalkaline subsurface and spring waters in Oman. While it is common to infer that H_2 production is associated with Fe(III) incorporation into serpentine (or magnetite) (e.g. Andreani et al., 2013; Klein et al., 2014; Bonnemains et al., 2016), a direct link between the processes proposed here and modern-day Fe transformations that are responsible for the H_2 currently measured in the subsurface of Oman remains elusive. We cannot be certain that the formation of Fe(III)-bearing serpentine led to H_2 production because we do not definitively know the conditions of reaction.

To further constrain the mechanisms of Fe transformations and H_2 production, it is necessary to acquire an appropriate suite of rocks and their corresponding fluids. Obtaining a representative suite of less to more reacted rocks sampled from the subsurface of Oman, out of contact with atmosphere, will allow us to rule out the possibility that oxygen and/or nitrate were the predominant oxidants interacting with the rocks. Complementary fluid samples and detailed aqueous and gaseous chemical analyses will help to further constrain the reaction pathways. An accurate mass balance for iron will allow us to expand our ability to assess the potential for H_2 production in such dynamic systems. Further development of quantitative methods to assess the oxidation state of iron in the diverse and complex mineral assemblages described here is necessary and underway.

ACKNOWLEDGEMENTS

We gratefully acknowledge Tyler Kane and Kate Campbell (USGS – Boulder, CO) for XRF analyses. We thank Franck Bourdelle (Université des Sciences et Technologies de Lille 1, France) and Manuel Muñoz (Université de Montpellier, France) for generously donating standards for calibration of the Fe(II/III) ratio of Fe K-edge XANES. We thank Julien Allaz for help with electron microprobe analyses conducted in the Department of Geological Sciences, University of Colorado at Boulder. Raman spectroscopy was conducted at the Raman Microspectroscopy Laboratory at the Department of Geological Sciences, University of Colorado-Boulder. This research was primarily funded by the Department of Energy (DE-SC0006886), with supporting work provided through the Rock-Powered Life NASA Astrobiology Institute (Cooperative Agreement NNA15BB02A). Use of the Stanford Synchrotron Radiation Lightsource, SLAC National Accelerator Laboratory, is supported by the U.S. Department of Energy, Office of Science, Office of Basic Energy Sciences under Contract No. DE-AC02-76SF00515, and was conducted in collaboration with staff scientists Sam Webb, Courtney Krest, and Ryan Davis.

APPENDIX A. SUPPLEMENTARY MATERIAL

Supplementary data associated with this article can be found, in the online version, at https://doi.org/10.1016/j.gca.2017.11.023.

REFERENCES

Andreani M., Grauby O., Baronnet A. and Muñoz M. (2008) Occurrence, composition and growth of polyhedral serpentine. *Eur. J. Mineral.* **20**, 159–171.

Andreani M., Munoz M., Marcaillou C. and Delacour A. (2013) Mu XANES study of iron redox state in serpentine during oceanic serpentinization. *Lithos* **178**, 70–83.

Andrew J. J. and Hancewicz T. M. (1998) Rapid analysis of raman image data using two-way multivariate curve resolution. *Appl. Spectrosc.* **52**, 797–807.

Bach W. (2016) Some compositional and kinetic controls on the bioenergetic landscapes in oceanic basement. *Front Microbiol.* **7**.

Bach W., Garrido C. J., Paulick H., Harvey J. and Rosner M. (2004) Seawater-peridotite interactions: First insights from ODP Leg 209, MAR 15 degrees N. *Geochem. Geophys. Geosyst.* **5**, 22.

Bach W. and Klein F. (2009) The petrology of seafloor rodingites: Insights from geochemical reaction path modeling. *Lithos* **112**, 103–117.

Bach W., Paulick H., Garrido C. J., Ildefonse B., Meurer W. P. and Humphris S. E. (2006) Unraveling the sequence of serpentinization reactions: petrography, mineral chemistry, and petrophysics of serpentinites from MAR 15 degrees N (ODP Leg 209, Site 1274). *Geophys. Res. Lett.* **33**.

Barnes I., O'neil J. R. and Trescases J.-J. (1978) Present day serpentinization in New Caledonia, Oman and Yugoslavia. *Geochim. Cosmochim. Acta* **42**, 144–145.

Barnes I. and O'Neill J. R. (1969) The relationship between fluids in some fresh alpine-type ultramafics and possible modern serpentinization, western United States. *Geol. Soc. Am. Bull.* **80**, 1947–1960.

Baronnet, A., Boudier, F., 2001. Microstructural and microchemical aspects of serpentinization. In: Eleventh Annual V. M. Goldschmidt Conference.

Beard J. S. and Frost B. R. (2016) The stoichiometric effects of ferric iron substitutions in serpentine from microprobe data. *Int. Geol. Rev.*, 1–7.

Beard J. S., Frost B. R., Fryer P., McCaig A., Searle R., Ildefonse B., Zinin P. and Sharma S. K. (2009) Onset and Progression of Serpentinization and Magnetite Formation in Olivine-rich Troctolite from IODP Hole U1309D. *J. Petrol.*, egp004.

Bonnemains D., Carlut J., Escartín J., Mével C., Andreani M. and Debret B. (2016) Magnetic signatures of serpentinization at ophiolite complexes. *Geochem. Geophys. Geosystems* **17**, 2969–2986.

Bosch D., Jamais M., Boudier F., Nicolas A., Dautria J.-M. and Agrinier P. (2004) Deep and high-temperature hydrothermal circulation in the oman ophiolite—petrological and isotopic evidence. *J. Petrol.* **45**, 1181–1208.

Boudier F., Baronnet A. and Mainprice D. (2010) Serpentine mineral replacements of natural olivine and their seismic implications: oceanic lizardite versus subduction-related antigorite. *J. Petrol.* **51**, 495–512.

Boudier F. and Coleman R. G. (1981) Cross section through the peridotite in the Samail Ophiolite, southeastern Oman Mountains. *J. Geophys. Res. Solid Earth* **86**, 2573–2592.

Cannat, M., Fontaine, F., Escartí, N.J., 2010. Serpentinization and associated hydrogen and methane fluxes at slow spreading ridges. In: Rona, P.A., Devey, C.W., Dyment, J., Murton, B.J., (Eds.), Diversity of Hydrothermal Systems on Slow Spreading Ocean Ridges. American Geophysical Union, pp. 241–264.

Clark I. D. and Fontes J.-C. (1990) Paleoclimatic reconstruction in northern Oman based on carbonates from hyperalkaline groundwaters. *Quat. Res.* **33**, 320–336.

D'Antonio M. and Kristensen M. B. (2004) Serpentine and brucite of ultramafic clasts from the South Chamorro Seamount (Ocean Drilling Program Leg 195, Site 1200): inferences for the serpentinization of the Mariana forearc mantle. *Mineral. Mag.* **68**, 887–904.

Debret B., Millet M.-A., Pons M.-L., Bouilhol P., Inglis E. and Williams H. (2016) Isotopic evidence for iron mobility during subduction. *Geology* **44**, 215–218.

Dewandel B., Lachassagne P., Boudier F., Al-Hattali S., Ladouche B., Pinault J.-L. and Al-Suleimani Z. (2005) A conceptual hydrogeological model of ophiolite hard-rock aquifers in Oman based on a multiscale and a multidisciplinary approach. *Hydrogeol. J.* **13**, 708–726.

Eckstrand O. R. (1975) The Dumont serpentinite; a model for control of nickeliferous opaque mineral assemblages by alteration reactions in ultramafic rocks. *Econ. Geol.* **70**, 183–201.

Evans B. W. (2008) Control of the products of serpentinization by the (FeMg1)-Mg-2 exchange potential of olivine and orthopyroxene. *J. Pet.* **49**, 1873–1887.

Evans B. W., Kuehner S. M. and Chopelas A. (2009) Magnetite-free, yellow lizardite serpentinization of olivine websterite, Canyon Mountain complex, NE Oregon. *Am. Mineral.* **94**, 1731–1734.

Evans B. W. and Trommsdorf V. (1972) Die einfluss des eisens auf die hydratisierung von duniten. *Schweiz. Mineral. Petrogr.* **52**, 251–256.

Falk E. S. and Kelemen P. B. (2015) Geochemistry and petrology of listvenite in the Samail ophiolite, Sultanate of Oman: Complete carbonation of peridotite during ophiolite emplacement. *Geochim. Cosmochim. Acta* **160**, 70–90.

Frost B. (1985) On the stability of sulfides, oxides, and native metals in serpentinite. *J. Petrol.* **26**, 31–63.

Frost B. R., Evans K. A., Swapp S. M., Beard J. S. and Mothersole F. E. (2013) The process of serpentinization in dunite from New Caledonia. *Lithos* **178**, 24–39.

Fujii T., Moynier F., Blichert-Toft J. and Albarède F. (2014) Density functional theory estimation of isotope fractionation of Fe, Ni, Cu, and Zn among species relevant to geochemical and biological environments. *Geochim. Cosmochim. Acta* **140**, 553–576.

Godard M., Jousselin D. and Bodinier J.-L. (2000) Relationships between geochemistry and structure beneath a palaeo-spreading centre: a study of the mantle section in the Oman ophiolite. *Earth Planet. Sci. Lett.* **180**, 133–148.

Hanghoj K., Kelemen P. B., Hassler D. and Godard M. (2010) Composition and genesis of depleted mantle peridotites from the Wadi Tayin Massif, Oman ophiolite; Major and trace element geochemistry, and Os isotope and PGE systematics. *J. Petrol.* **51**, 201–227.

Harrison A. L., Dipple G. M., Power I. M. and Mayer K. U. (2015) Influence of surface passivation and water content on mineral reactions in unsaturated porous media: Implications for brucite carbonation and CO2 sequestration. *Geochim. Cosmochim. Acta* **148**, 477–495.

Harrison A. L., Power I. M. and Dipple G. M. (2013) Accelerated carbonation of brucite in mine tailings for carbon sequestration. *Environ. Sci. Technol.* **47**, 126–134.

Hoal K. O., Stammer J. G., Appleby S. K., Botha J., Ross J. K. and Botha P. W. (2009) Research in quantitative mineralogy: Examples from diverse applications. *Miner. Eng.* **22**, 402–408.

Hostetler P. B., Coleman R. G. and Evans B. W. (1966) Brucite in alpine serpentinites. *Am. Mineral.* **51**, 75–98.

Kahl W.-A., Jöns N., Bach W., Klein F. and Alt J. C. (2015) Ultramafic clasts from the South Chamorro serpentine mud volcano reveal a polyphase serpentinization history of the Mariana forearc mantle. *Lithos* **227**, 1–20.

Katayama I., Kurosaki I. and Hirauchi K. (2010) Low silica activity for hydrogen generation during serpentinization: An example of natural serpentinites in the Mineoka ophiolite complex, central Japan. *Earth Planet. Sci. Lett.* **298**, 199–204.

Kelemen P. B. and Matter J. (2008) In situ carbonation of peridotite for CO2 storage. *Proc. Natl. Acad. Sci.* **105**, 17295–17300.

Kelemen P. B., Matter J., Streit E. E., Rudge J. F., Curry W. B. and Blusztajn J. (2011) Rates and mechanisms of mineral carbonation in peridotite: natural processes and recipes for enhanced, in situ CO(2) capture and storage RID A-2653-2012. In *Annual Review of Earth and Planetary Sciences*, vol. 39 (eds. R. Jeanloz and K. Freeman). Annual Reviews, Palo Alto, pp. 545–576.

Klein F., Bach W., Humphris S. E., Kahl W.-A., Jons N., Moskowitz B. and Berquo T. S. (2014) Magnetite in seafloor serpentinite–Some like it hot. *Geology* **42**, 135–138.

Klein F., Bach W., Jons N., McCollom T., Moskowitz B. and Berquó T. (2009) Iron partitioning and hydrogen generation during serpentinization of abyssal peridotites from 15 N on the Mid-Atlantic Ridge. *Geochim. Cosmochim. Acta* **73**, 6868–6893.

Klein F., Bach W. and McCollom T. M. (2013) Compositional controls on hydrogen generation during serpentinization of ultramafic rocks. *Lithos* **178**, 55–69.

Lafay R., Montes-Hernandez G., Janots E., Chiriac R., Findling N. and Toche F. (2012) Mineral replacement rate of olivine by chrysotile and brucite under high alkaline conditions. *J. Cryst. Growth* **347**, 62–72.

Lafuente B., Downs R., Yang H. and Stone N. (2015) The power of databases: the RRUFF project. In *Highlights in Mineralogical Crystallography* (eds. T. Armbruster and R. Danisi). W. De Gruyter, Berlin, Germany, pp. 1–30.

Malvoisin, B., Brunet, F., Carlut, J., Roumejon, S., Cannat, M., 2012. Serpentinization of oceanic peridotites: 2. Kinetics and processes of San Carlos olivine hydrothermal alteration. J. Geophys. Res.-Solid Earth, 117.

Malvoisin B., Carlut J. and Brunet F. (2012) Serpentinization of oceanic peridotites: 1. A high-sensitivity method to monitor magnetite production in hydrothermal experiments. *J. Geophys. Res. Solid Earth* **117**, B01104.

Marcaillou C., Muñoz M., Vidal O., Parra T. and Harfouche M. (2011) Mineralogical evidence for H2 degassing during serpentinization at 300 °C/300 bar. *Earth Planet. Sci. Lett.*.

Mayhew L. E., Ellison E. T., McCollom T. M., Trainor T. P. and Templeton A. S. (2013) Hydrogen generation from low-temperature water-rock reactions. *Nat. Geosci.* **6**, 478–484.

Mayhew L. E., Webb S. M. and Templeton A. S. (2011) Microscale imaging and identification of Fe speciation and distribution during fluid-mineral reactions under highly reducing conditions. *Environ. Sci. Technol.* **45**, 4468–4474.

McCollom T. M. and Bach W. (2009) Thermodynamic constraints on hydrogen generation during serpentinization of ultramafic rocks. *Geochim. Cosmochim. Acta* **73**, 856–875.

McCollom T. M., Klein F., Robbins M., Moskowitz B., Berquó T. S., Jöns N., Bach W. and Templeton A. (2016) Temperature trends for reaction rates, hydrogen generation, and partitioning of iron during experimental serpentinization of olivine. *Geochim. Cosmochim. Acta* **181**, 175–200.

Miller H. M., Matter J. M., Kelemen P., Ellison E. T., Conrad M. E., Fierer N., Ruchala T., Tominaga M. and Templeton A. S. (2016) Modern water/rock reactions in Oman hyperalkaline peridotite aquifers and implications for microbial habitability. *Geochim. Cosmochim. Acta* **179**, 217–241.

Miller H. M., Mayhew L. E., Ellison E. T., Kelemen P., Kubo M. and Templeton A. S. (2017) Low temperature hydrogen production during experimental hydration of partially-serpentinized dunite. *Geochim. Cosmochim. Acta* **209**, 161–183.

Miyoshi A., Kogiso T., Ishikawa N. and Mibe K. (2014) Role of silica for the progress of serpentinization reactions: Constraints from successive changes in mineralogical textures of serpentinites from Iwanaidake ultramafic body, Japan. *Am. Mineral.* **99**, 1035–1044.

Monnier C., Girardeau J., Le Mée L. and Polvé M. (2006) Along-ridge petrological segmentation of the mantle in the Oman ophiolite. *Geochem. Geophys. Geosyst.* **7**, Q11008.

Moody J. B. (1976) An experimental study on the serpentinization of iron-bearing olivines. *Can. Miner.* **14**, 462–478.

Moody J. B. (1976) Serpentinization: a review. *Lithos* **9**, 125–138.

Munoz M. O. V. (2013) Iron oxidation state in phyllosilicate single crystals using Fe-K pre-edge and XANES spectroscopy: Effects of the linear polarization of the synchrotron X-ray beam. *Am. Mineral.* **98**, 1187–1197.

Neal C. and Stanger G. (1983) Hydrogen generation from mantle source rocks in Oman. *Earth Planet. Sci. Lett.* **66**, 315–320.

Neal C. and Stanger G. (1985) Past and present serpentinisation of ultramafic rocks; an example from the semail ophiolite nappe of Northern Oman. In *The Chemistry of Weathering* (ed. J. I. Drever). Nato ASI Series. Springer, Netherlands, pp. 249–275.

Nealson K. H., Inagaki F. and Takai K. (2005) Hydrogen-driven subsurface lithoautotrophic microbial ecosystems (SLiMEs): do they exist and why should we care? *Trends Microbiol.* **13**, 405–410.

Nisbet E. G. and Sleep N. H. (2001) The habitat and nature of early life. *Nature* **409**, 1083–1091.

Newville M. (1998) *FEFFIT, Using FEFF to model XAS data*. Argonne National Lab, University of Chicago, APS. Available at: http://cars.uchicago.edu/~newville/feffit/feffit.pdf.

O'Day P., Rivera N., Root R. and Carroll S. (2004) X-ray absorption spectroscopic study of Fe reference compounds for the analysis of natural sediments. *Am. Mineral.* **89**, 572–585.

Ogasawara Y., Okamoto A., Hirano N. and Tsuchiya N. (2013) Coupled reactions and silica diffusion during serpentinization. *Geochim. Cosmochim. Acta* **119**, 212–230.

O'Hanley D. S. and Dyar M. (1993) The composition of lizardite 1T and the formation of magnetite in serpentinites. *Am. Mineral.* **78**, 391–404.

Okamoto A., Ogasawara Y., Ogawa Y. and Tsuchiya N. (2011) Progress of hydration reactions in olivine–H2O and orthopyroxenite–H2O systems at 250 & #xB0;C and vapor-saturated pressure. *Chem. Geol.* **289**, 245–255.

Ostergren J., Brown G., Parks G. and Tingle T. (1999) Quantitative speciation of lead in selected mine tailings from Leadville, CO. *Environ. Sci. Technol.* **33**, 1627–1636.

Oufi O., Cannat M. and Horen H. (2002) Magnetic properties of variably serpentinized abyssal peridotites. *J. Geophys. Res.-Solid Earth*, 107.

Page N. J. (1967) Serpentinization at Burro Mountai, California. *Contrib. Mineral. Petrol.* **14**, 321–342.

Paukert A. N., Matter J. M., Kelemen P. B., Shock E. L. and Havig J. R. (2012) Reaction path modeling of enhanced in situ CO2 mineralization for carbon sequestration in the peridotite of the Samail Ophiolite, Sultanate of Oman. *Chem. Geol.* **330–331**, 86–100.

R Development Core Team, 2013. R - A Language and Environment for Statistical Computing.

Rempfert K. R., Miller H. M., Bompard N., Nothaft D., Matter J. M., Kelemen P., Fierer N. and Templeton A. S. (2017) Geological and geochemical controls on subsurface microbial life in the samail ophiolite. *Front. Microbiol.* **8**.

Reynard B., Bezacier L. and Caracas R. (2015) Serpentines, talc, chlorites, and their high-pressure phase transitions: a Raman spectroscopic study. *Phys. Chem. Miner.* **42**, 641–649.

Russell M. J., Hall A. J. and Martin W. (2010) Serpentinization as a source of energy at the origin of life. *Geobiology* **8**, 355–371.

Schwarzenbach E. M., Caddick M. J., Beard J. S. and Bodnar R. J. (2016) Serpentinization, element transfer, and the progressive development of zoning in veins: evidence from a partially serpentinized harzburgite. *Contrib. Mineral. Petrol.* **171**, 5.

Seyfried W. E., Foustoukos D. I. and Fu Q. (2007) Redox evolution and mass transfer during serpentinization: An experimental and theoretical study at 200 degrees C, 500 bar with implications for ultramafic-hosted hydrothermal systems at Mid-Ocean Ridges. *Geochim. Cosmochim. Acta* **71**, 3872–3886.

Sleep N. H., Meibom A., Fridriksson T., Coleman R. G. and Bird D. K. (2004) H-2-rich fluids from serpentinization: Geochemical and biotic implications. *Proc. Natl. Acad. Sci. U. S. A.* **101**, 12818–12823.

Streit E., Kelemen P. and Eiler J. (2012) Coexisting serpentine and quartz from carbonate-bearing serpentinized peridotite in the Samail Ophiolite, Oman. *Contrib. Mineral. Petrol.* **164**, 821–837.

Toft P. B., Arkani-Hamed J. and Haggerty S. E. (1990) The effects of serpentinization on density and magnetic susceptibility: a petrophysical model. *Phys. Earth Planet. Inter.* **65**, 137–157.

Webb S. M. (2005) SIXPack: a graphical user interface for XAS analysis using IFEFFIT. *Phys. Scr.* **2005**, 1011.

Whittaker E. and Wicks F. J. (1970) Chemical differences among serpentine polymorphs - A discussion. *Am. Mineral.* **55**, 1025.

Wilke M., Farges F., Petit P.-E., Brown G. E. and Martin F. (2001) Oxidation state and coordination of Fe in minerals: An Fe K-XANES spectroscopic study. *Am. Mineral.* **86**, 714–730.

Associate editor: Wolfgang Bach